LAWRENCE
LIVERMORE
NATIONAL
LABORATORY

LLNL-BOOK-433853

Heat Capacity Lasers

M. Rotter, R. Yamamoto

June 1, 2010

High Power Laser Handbook

Disclaimer

This document was prepared as an account of work sponsored by an agency of the United States government. Neither the United States government nor Lawrence Livermore National Security, LLC, nor any of their employees makes any warranty, expressed or implied, or assumes any legal liability or responsibility for the accuracy, completeness, or usefulness of any information, apparatus, product, or process disclosed, or represents that its use would not infringe privately owned rights. Reference herein to any specific commercial product, process, or service by trade name, trademark, manufacturer, or otherwise does not necessarily constitute or imply its endorsement, recommendation, or favoring by the United States government or Lawrence Livermore National Security, LLC. The views and opinions of authors expressed herein do not necessarily state or reflect those of the United States government or Lawrence Livermore National Security, LLC, and shall not be used for advertising or product endorsement purposes.

Laser Equations

The geometry we wish to consider is shown in Figure 1. The (one-dimensional) laser medium is compoased of *m* slabs, eqach with a thickness of ℓ between two mirrors or reflectivity R_1 and R_2. The cavity defined by the mirrors has length L_{cav} and the total length of the active medium is $L_{slab} = m\ell$. Each slab surface is pumped at an intensity $i_p(\lambda,t)$ W/cm²-nm. For simplicity, we'll assume the laser output is on a single line. Within the medium there are circulating intensities $I_L^{\pm}$ (W/cm²) and the medium has a bulk loss α (cm⁻¹).

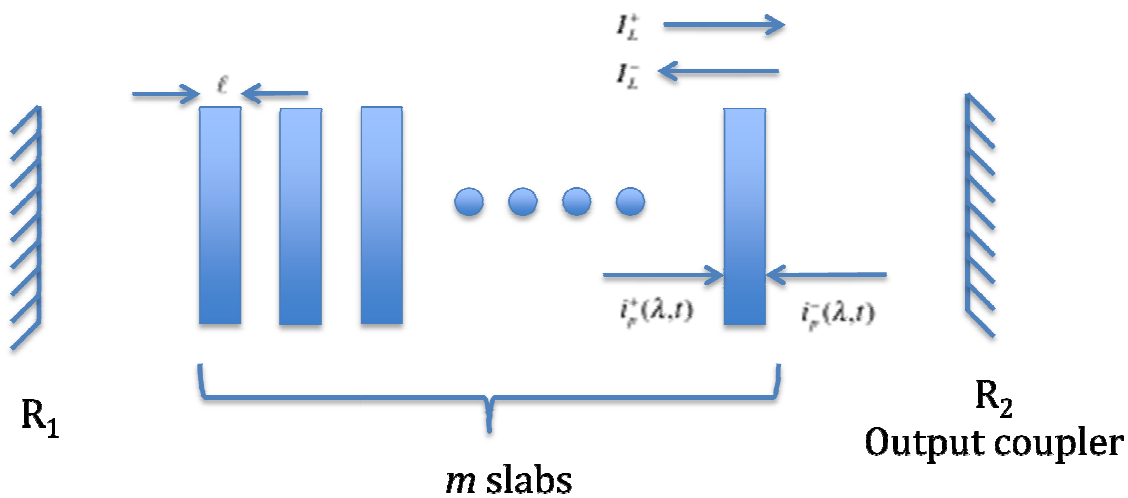

Figure 1: Geometry of the SSHCL used in the model

The absorption cross-section of Nd:YAG in the vicinity of the 808 nm pump band is shown in Figure 2, along with the time-integrated pump sepectrum. As may be seen, there are numerous peaks and valleys in the cross-section spectrum. In addition, the pump laser diodes themselves have a time-dependent center wavelength and spectral width. It is therefore important to use the more general expression for the pump rate into the upper laser level, *i.e.*,

$$R_p(z,t) \propto \int \lambda\sigma_a(\lambda) i_p(\lambda,t)[\exp(-N_0\sigma_a(\lambda)z) + \exp(-N_0\sigma_a(\lambda)(\ell - z))]d\lambda$$

where $\sigma_a(\lambda)$ is the absorption cross-section, N_0 is the Nd concentration in the ground state, and the integral is done over the pump band (typically 800 to 820 nm). Implicit in the above is the assumption that both surfaces of the slab see the same pump intensity.

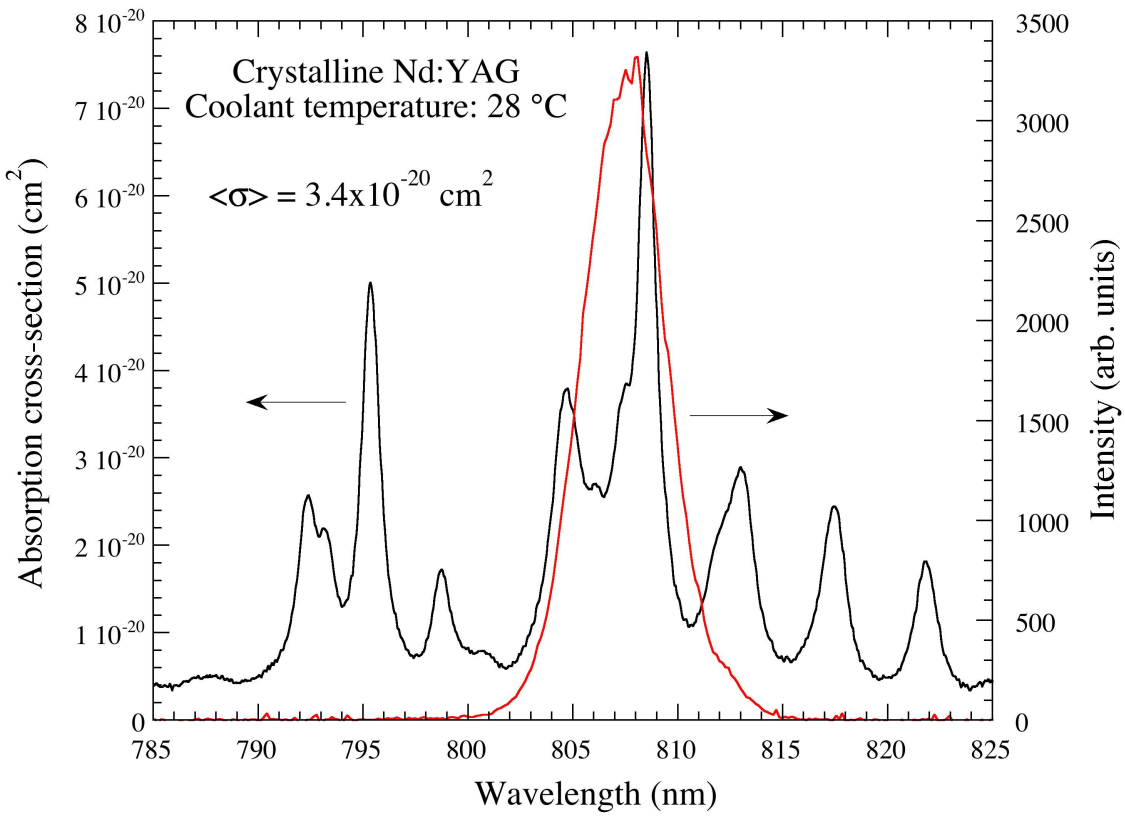

Figure 2: The 808 nm absorption band of Nd:YAG. Superimposed in red is the time-integrated laser diode pump spectrum.

The instantaneous pump spectral intensity, $i_p(\lambda,t)$, may be further written as

$$i_p(\lambda,t) = f_p(t)\exp[-4\ln 2(\lambda - \lambda_c(t))^2 / \Delta\lambda^2(t)]$$

where $f_p(t)$ describes the overall pump profile,

$$\lambda_c(t) = A[1 - e^{Bt}\mathrm{erfc}(\sqrt{Bt})]$$

is the center wavlength, with *A* and *B* fit coefficients, and $\Delta\lambda(t) = 2.7 + t/235$ nm is the spectral FWHM, with t in μs.

Since there will be considerable heat build-up in the lasing medium, we need to take into account the thermal population of the lower laser level as well as the thermal depopulation of the upper level. The energy level diagram of interest is shown in Figure 3. Since we are dealing with a four-level laser system, the decay out of level 3 into level 2 (and likewise for level 1 into level 0) is extremely rapid on the time scales of interest; levels 3 and 2 (and levels 1 and 0) are in thermodynamic equilibrium. Consequently, if ΔE_{10} and ΔE_{32} are the energy differences between levels 1,0 and 3,2 respectively, we may write the populations of levels 1 and 2 at temperature *T* as

$$N_1(T) = N_0 e^{-\Delta E_{10}/kT}$$

where ΔE_{10} = 0.26 eV, and *k* is Boltzmann's constant. Likewise the population of level 2 at temperature *T* is

$$N_2^0(T) = \frac{Z_{32}(T)}{Z_{32}(T_0)} N_2^0(T_0)$$

where T_0 is the reference temperature and

$$Z_{32}(T) = \frac{Z_2(T)}{Z_2(T) + Z_3(T)}$$

is the fraction of atoms in level 2. The population $N_2^0(T)$ refers to the population of level 2 by the pump process at temperature *T*. It is to be distinguished from the purely thermal population $N_2(T)$ which, because of its position relative to the ground state, is effectively zero. The partition functions Z_2 and Z_3 in Eq. (xx) are defined as

$$Z_i(T) = \sum_\alpha e^{-E_{i\alpha}/kT}$$

where α labels the sublevels of level *i*. We find Z_{32} is to good approximation (erlandson)

$$Z_{32}(T) = 1/[1 + 4\exp(-\Delta E_{32}/kT)]$$

where ΔE_{32} = 0.13 eV.

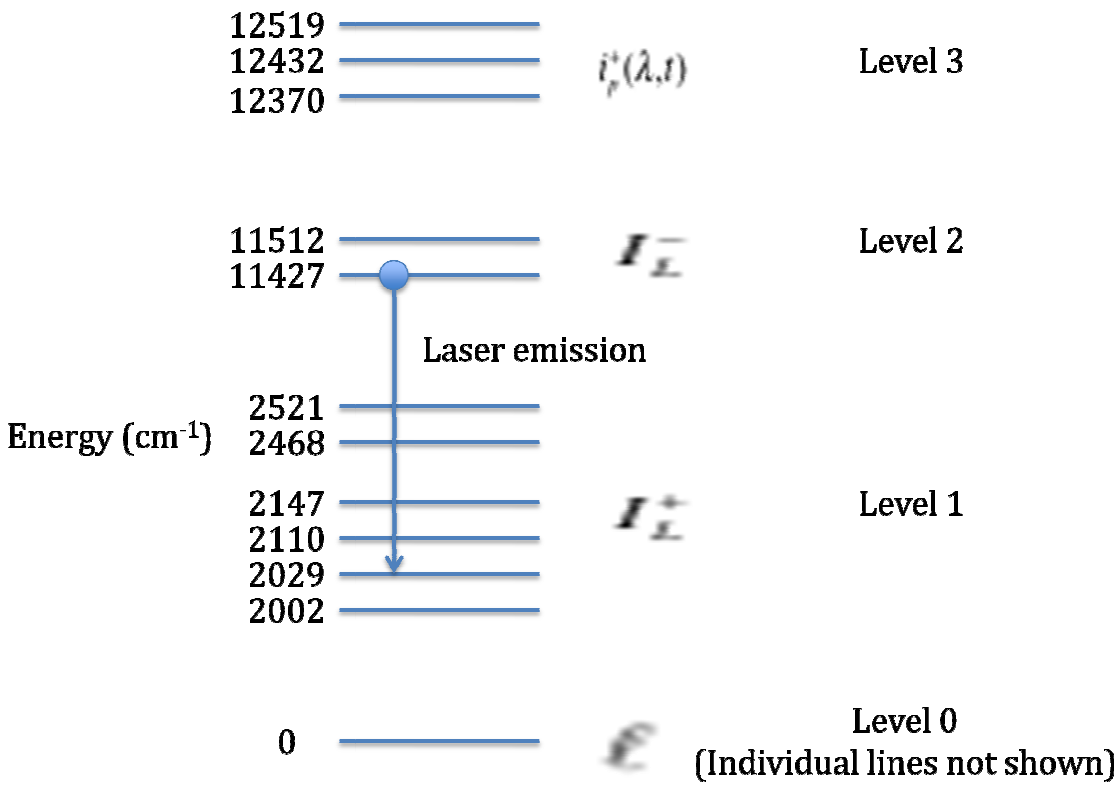

Figure 3: Energy-level diagrom of Nd:YAG showing the levels considered in the model. Pumping is into the $^4F_{5/2}$ band.

The equations describing the oscillator can then be given as

$$\frac{\partial N_2^0(T)}{\partial t} = \frac{N_0}{hc} R_p(z,t) - k_T N_2^0(T) - \frac{(\sigma_{21}(T)N_2^0(T) - \sigma_{12}(T)N_1(T))(I_L^+ + I_L^-)}{h\nu_L}$$

$$\pm\frac{\partial I_L^\pm}{\partial z} + \frac{n}{c}\frac{\partial I_L^\pm}{\partial t} = [(\sigma_{21}(T)N_2^0(T) - \sigma_{12}(T)N_1(T))(I_L^\pm + I_n^\pm) - \alpha I_L^\pm](L_{slab} / L_{cav})$$

where k_T is the total decay rate out of the upper laser level, *i.e.* $k_T = k_F + k_{ASE}$, where k_F is the fluorescence decay rate and k_{ASE} is the decay rate due to Amplified Spontaneous Emission (ASE, see below). The noise term that initiatiates the lasing process is given by $I_n^\pm$ and any distributed loss in the system is given by the parameter α. The above system is closed by noting that $N_0 + N_2 = N$, where N is the total Nd concentration. The initial/boundary conditions are

$$N_2^0(t=0) = I_L^\pm(t=0) = 0$$

$$I_L^+(z=0,t) = R_1 I_L^-(z=0,t) \qquad \text{and} \qquad I_L^-(z=L_{cav},t) = R_2 I_L^+(z=L_{cav},t)$$

where R_1 is the high-reflector reflectivity and R_2 is the output coupler reflectivity.

As an example of the results obtained with these calculations, we show in Figure 4 the spatially-averaged gain coefficient, the output intensity, and output fluence as a function of time for a four-slab Nd:YAG system.

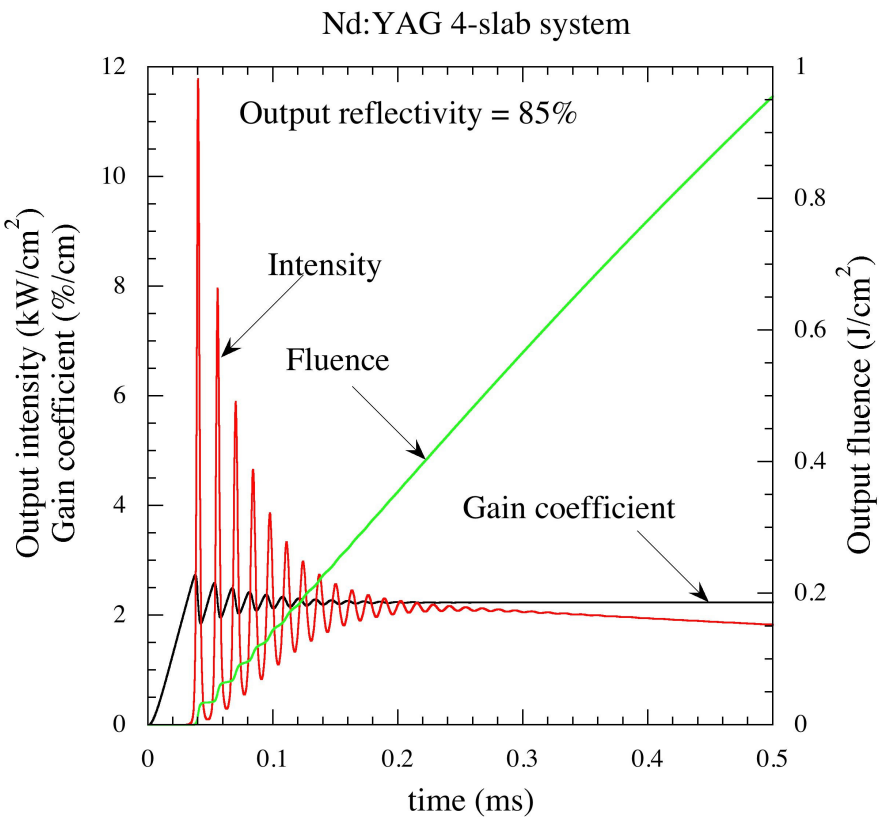

Figure 4: Calculated output variables for a four-slab Nd:YAG oscillator.

The presence of relaxation oscillations is readily apparent, as is the clamping of the gain at threshold after a steady-state has been reached. For this case, the output fluence is approximately 1 J/cm^2. For an active region 100 cm^2 in area, this represents an output energy/pulse of about 100 J, or an average power of 20 kW at a 200 Hz repetition rate.

The spatially-dependent gain coefficient is shown in Figure 5 for the above case. The rapid absorption of the pump light near the surface of each slab is clearly visible in this case.

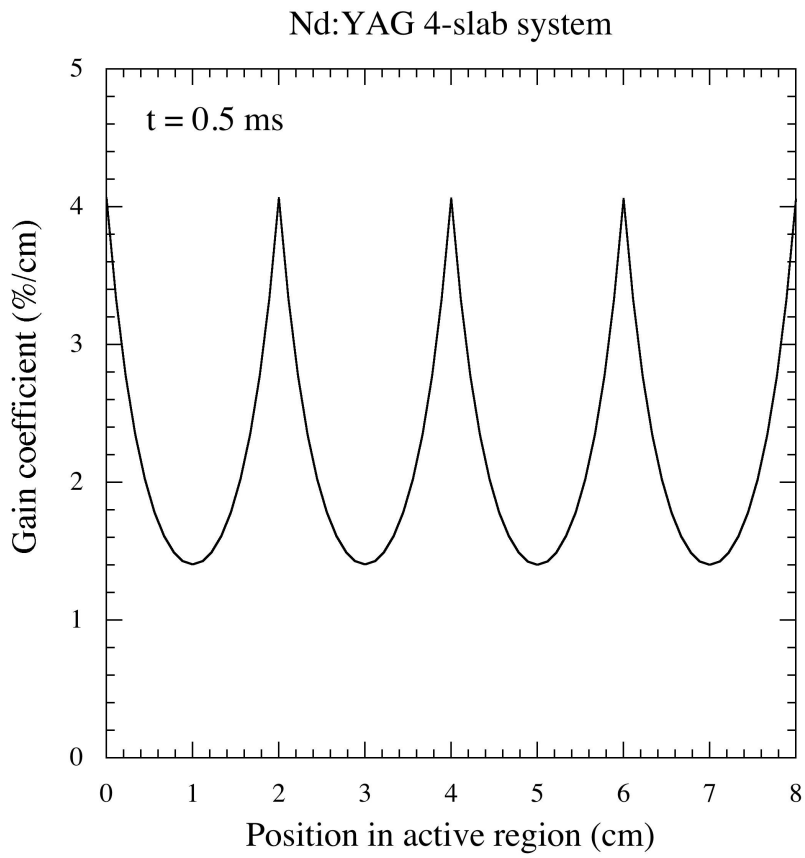

Figure 5: Spatially-dependent gain coefficient for the Nd:YAG 4-slab system. Results shown are taken at the end of the pulse, 0.5 ms.

As an example of the type of parameter studies that may be done, in Figure 6 we show the output power as a function of slab count and output coupler reflectivity. The equivalent unstable resonator magnification ($M = 1/\sqrt{R_{oc}}$) as well as the measured output power for the M = 1.5 case is shown as well. As expected, systems with higher slab count tend to optimize at higher values of magnification due to the increased amount of gain in the propagation direction.

Finally, we show in Figure 7 the dependence on output power on the temperature of the slab. As mentioned above, the output power is reduced as the temperature is increased due to thermal population of the lower laser level as well as thermal de-population of the upper laser level. The calculation shown is for a seven slab system, producing roughly 75 kW output power at the initial temperature of 300 ^{o}K. For relatively limited temperature increases of 100 ^{o}K, the output power at the end of the burst is about 80% of the initial power. We have found that a typical temperature rise/pulse is approximately 0.05 ^{o}K. Thus a ten-second burst at 200 Hz raises the temperature on the order of 100 ^{o}K.

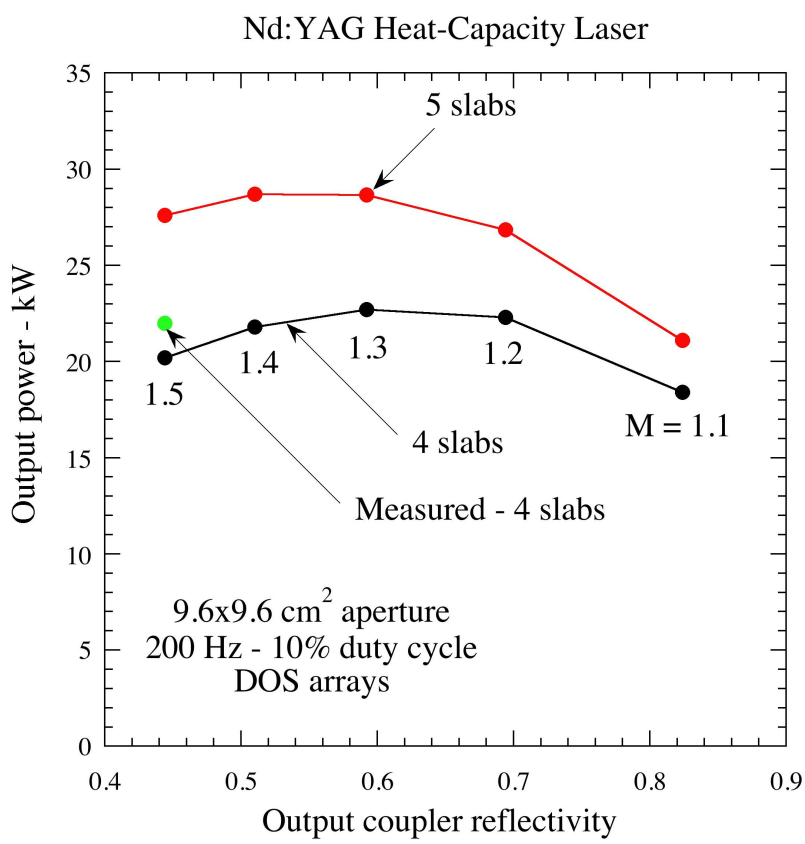

Figure 6: Output power as a function of output coupler reflectivity and slab count for a Nd:YAG heat-capacity laser.

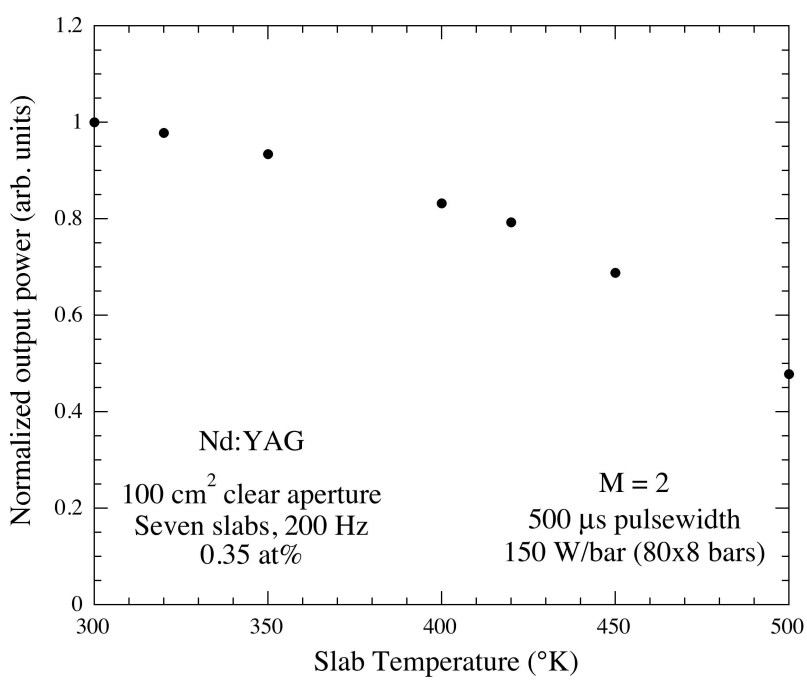

Figure 7: Output power as a function of slab temperature. Nominal output power at 300 °K is 75 kW.

The effects of Amplified Spontaneous Emission (ASE)

In a solid-state laser medium, a large fraction of the spontaneous emission is trapped due to total internal reflection. To absorb this radiation, and thus prevent internal parasitics from forming, edge claddings are placed around the perimeter of the material, as shown in Figure 8.

Figure 8: Ceramic Nd:YAG slab with Cobalt-doped, epoxy-bonded edge cladding.

The effect of ASE on stored energy may be modeled through an artifice called the "ASE multiplier," or M_{ase}. If no ASE were present in the slab, the upper laser level would decay at the fluorescence decay rate, $k_F = 1/t_F$, where t_F is the fluorescence lifetime. In the presence of ASE, the upper state will decay at a rate $k_{ASE} = k_F(M_{ASE} - 1)$, where $M_{ase} \geq 1$ and $M_{ase} = 1$ indicates no ASE. The ASE multiplier may be parameterized by the gain-width product, or the product of the gain coefficient (in cm^{-1}) with the width of the clear aperture (in cm) of the slab.

We used a Monte-Carlo 3-D ray-trace code[1] to calculate the ASE multiplier as a function of the gain-width product for a given slab geometry. The code launches rays at random positions and directions within the slab, keeping track of the gain (or loss) as the ray propagates through the slab. A parasitic condition is noted when $M_{ase} \to \infty$.

As mentioned above, we can parameterize the ASE multiplier in terms of the variable $\beta = gL$, where L is the width of the pumped region. In particular,

$$M_{ase} - 1 = \beta \exp\left(m_1 + m_2\beta + m_3\beta^2 + m_4\beta^3\right)$$

where the m_i are fit coefficients. An example of this type of calculation is shown in Figure 9 for a YAG slab of dimensions 10x10x2 cm^3 and assuming no index mismatch between the slab and the edge cladding.

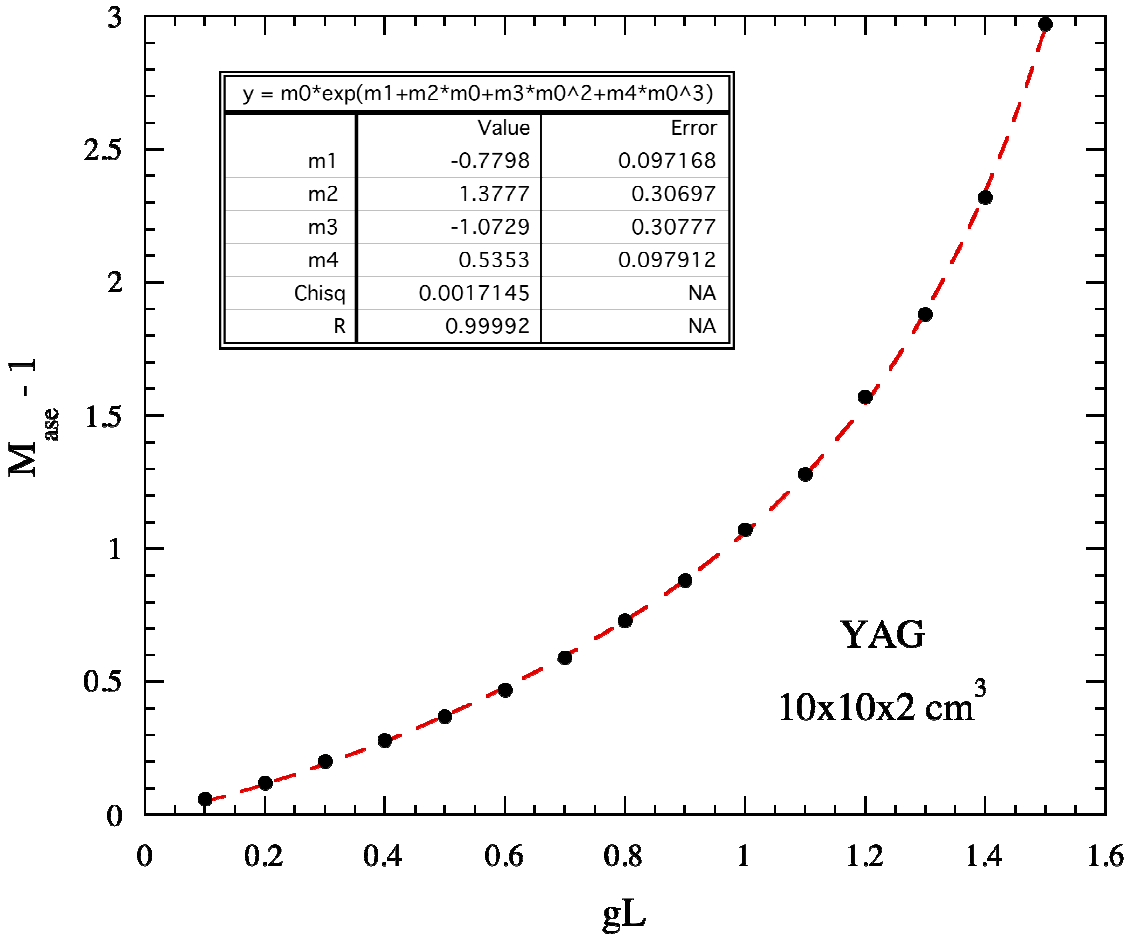

Figure 9: Variation of ASE multiplier with gain coefficient-width product and analytical fit

In the presence of ASE, the rate equation for the gain coefficient, g, (or, equivalently, the stored energy density) may be written as

$$\frac{dg}{dt} = P(t) - gM_{ase}(g)k_F$$

where $P(t)$ is the pump rate, and it has been explicitly noted that the ASE multiplier is a function of the gain coefficient. From the above equation, we see that large values of the ASE multiplier lead to a rapid (in time) reduction of the gain coefficient, and consequently of the stored energy density. Physically, the gain coefficient "clamps" at a given value. At this point, the pump energy goes into generating more ASE as opposed to increasing the gain coefficient.

Under ideal conditions, there would be no mismatch in refractive index between the slab and the edge cladding. This can be achieved by diffusion bonding

the edge cladding to the slab, or co-sintering the edge cladding to the slab in the case of ceramic media. Both of these approaches have proved to be time-consuming and not very repeatable in terms of yield.

Another approach is to use a bonding agent (such as epoxy) between the slab and the edge cladding. Unfortunately, most epoxies have a refractive index nowhere near that of YAG. The Fresnel reflection of spontaneous emission at the slab/epoxy interface easily leads to the formation of parasitics within the slab. If, however, the slab edge is roughened prior to bonding, the diffuse scattering that results acts to inhibit the formation of parasitics.

We can treat the roughened surface in our ASE model as follows. The surface is characterized by the variable $\zeta(x,y)$, which represents the difference in height (in the z-direction) at any point (x,y) from the mean z-value of the surface. We assume ζ is a normally-distributed, stationary, random process with zero mean and variance σ^2. The random distribution is further described by a correlation distance, T.

We shall also assume the surface is quite rough, so that $\sigma/\lambda >> 1$, where λ is the wavelength of the light. In this limit, the probability density for normally-incident light to be scattered into an angle θ may be written as[i]

$$p(\theta;\xi) = \frac{c\xi}{1+\cos\theta}\exp\left[-\frac{\xi^2\sin^2\theta}{8(1+\cos\theta)^2}\right]$$

where

$$c = \left[\sqrt{2\pi}\,\mathrm{erf}\left(\frac{\xi}{2\sqrt{2}}\right)\right]^{-1}$$

and $\xi = T/\sigma$ characterizes the surface. A rough surface is given by $\xi \to 0$; a smooth surface by $\xi \to \infty$. Each time a ray hits the edge of the slab, its new (reflected) direction is randomized according to the above probability distribution. If U represents a uniformly-distributed random number on (0,1), the scattering angle, θ, as given by the above probability density may be generated from[ii]

$$\theta(U;\xi) = 2\tan^{-1}\left\{\frac{2\sqrt{2}}{\xi}\mathrm{erf}^{-1}\left[U\,\mathrm{erf}\left(\frac{\xi}{2\sqrt{2}}\right)\right]\right\}$$

where erf^{-1} is the inverse error function.

Figure 10 shows the effect of epoxy refractive index on the ASE multiplier as a function of gain coefficient-width product. As expected, the closer the refractive index of the epoxy approaches that of the YAG slab (refractive index ~1.82), the less of an effect the epoxy has on the multiplier. The arrows indicate at what value of gain-width product parasitics begin to occur. In Figure 11 we show the measured and calculated gain coefficient of an epoxy-bonded edge cladding where the epoxy refractive index is 1.62. We see that eventually the slab develops parasitics, as

noted by the clamping of the gain coefficient at 0.11 cm^{-1}, but the operating point of our heat-capacity laser is well below this, as indicated by the dashed line.

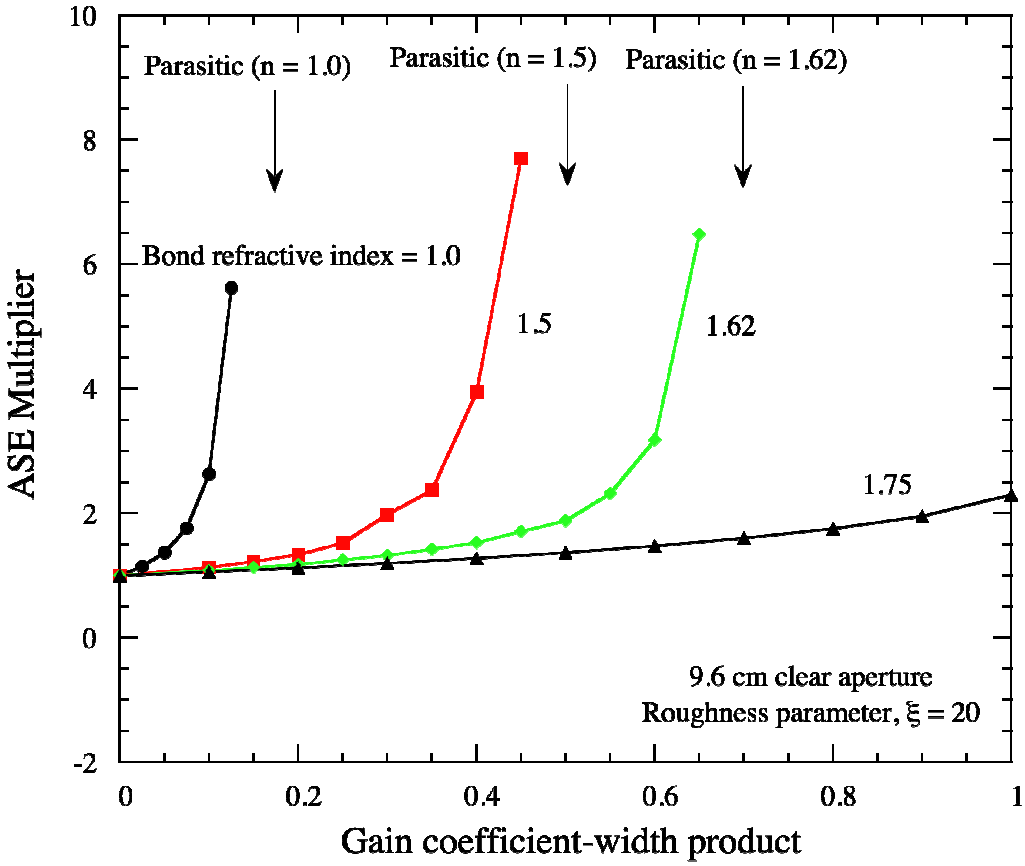

Figure 10: Effect of bond refractive index on ASE multiplier.

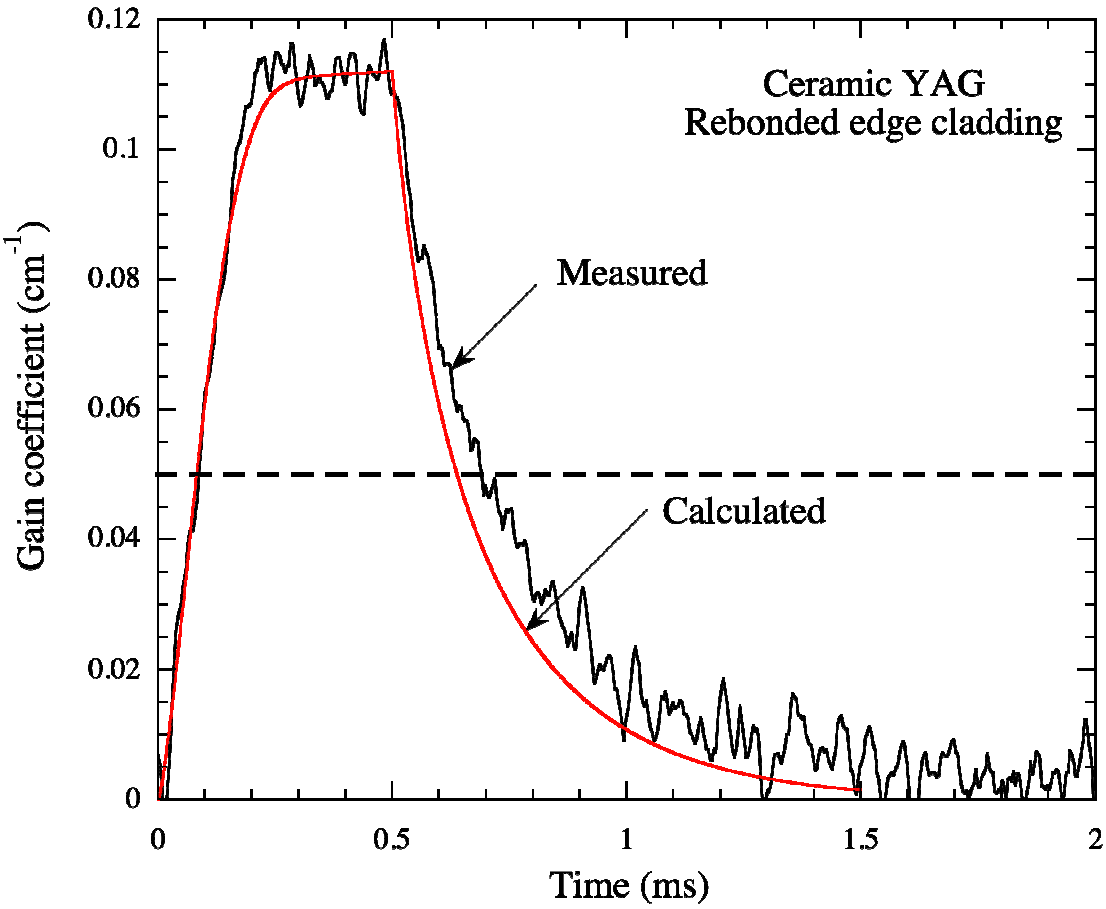

Figure 11: Measured and calculated gain coefficient for a ceramic YAG slab. Epoxy refractive index is 1.62. The dashed line indicates the operating point for a four-slab system with an unstable resonator magnification of 1.5.

Wavefront distortion

Even though the heat-capacity laser was designed to minimize thermal gradients, and hence thermally-induced wavefront distortion, gradients still exist transverse to the propagation direction due to non-uniformities in the pump illumination. In this section, we examine our approach to calculating these effects and how they limit the performance of the system.

The modeled geometry is shown in Figure 12. The teal region represents the ceramic Nd:YAG slab, with the red region denoting the Co:GGG edge cladding. In between the two regions is a 5 mil epoxy bond. Due to the thinness of the bond, this region does not show up in the figure. Also modeled is an air gap between two adjacent pieces of edge cladding. Again, because of the thinness of the gap, this region does not show up in the figure.

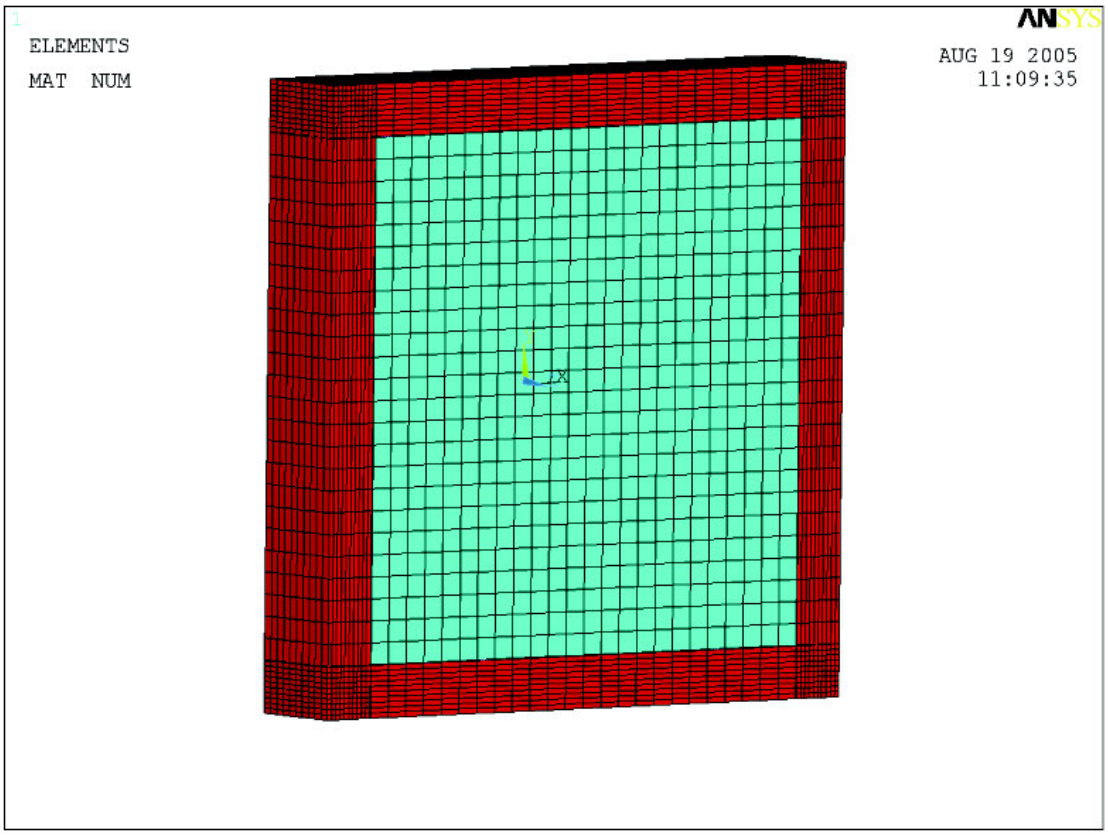

Figure 12: Geometry of modeled slab. The teal region is ceramic Nd:YAG, the red region is the Co:GGG edge cladding. In between the two regions is a thin (5 mil) epoxy layer, not visible in this picture

Thermal calculations

The thermo-elastic calculation begins with the specification of the thermal source function. To this end, for the YAG region, we used the actual measured laser diode array intensity profiles at the plane of the slab. For the edge cladding region, we assumed that the unextracted energy was depositied uniformly around the perimeter of the active region. The calculation was thus run for each slab in the laser individually since the diode array profiles were different for each slab. For both the YAG and GGG the temperature dependence of the thermal constants (notably thermal conductivity and specific heat) was taken into account. Time dependence was included for both the temperature and stress parts of the calculations.

The temperature distribution for slab #4 after five seconds is shown in Figure 13. The scale on the bottom is in °C, with an initial (uniform) temperature of 20 °C. We see that to a good approximation, the surface of the slab heats up at a rate of about 11-12 °C/sec. The non-uniformity of the diode light is readily apparent in this figure. One of the main drivers in generating depolarization is the X-Y shear stress. This quantity is shown in Figure 14 corresponding to the temperature

distribution in Figure 13. We see, as expected, that the greatest shear stress occurs in the corners of the slab, and thus this is where one would expect to see the greatest amount of depolarization.

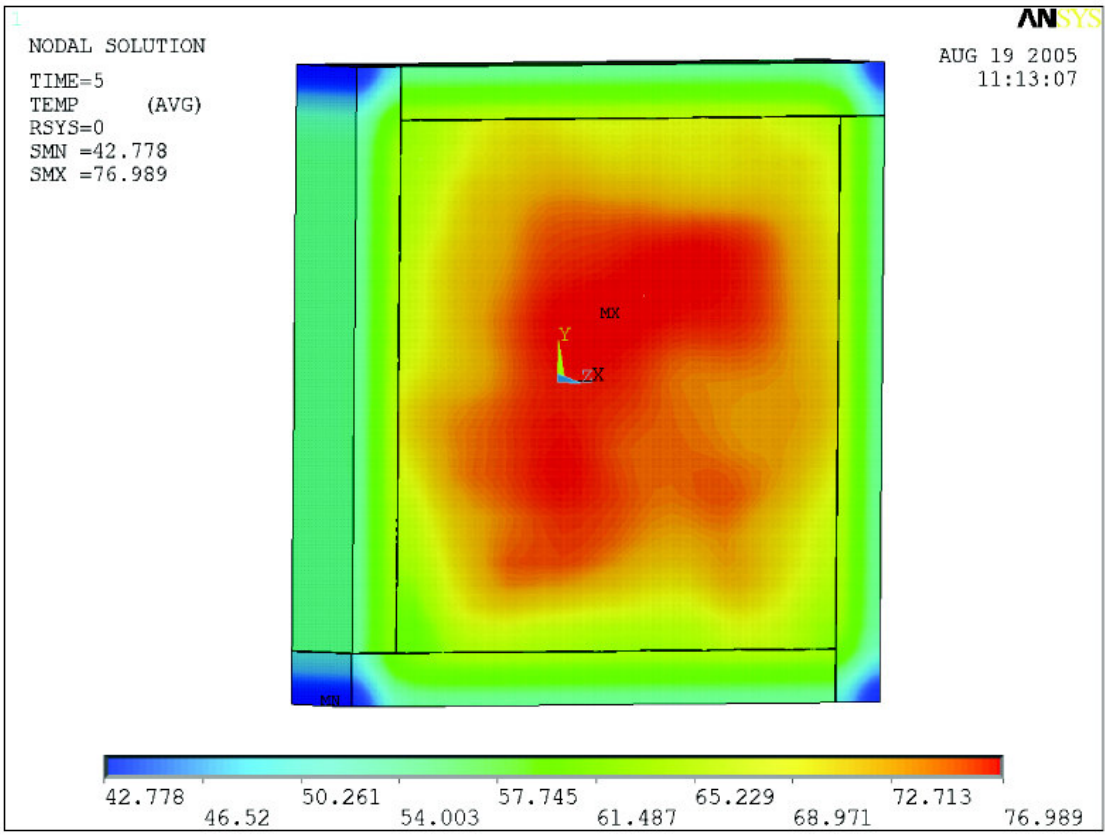

Figure 13: Temperature controus after five seconds. Scale is in °C.

With our FLIR thermal camera, we were able to measure the temperature at the surface of the slab, and thus compare the model predictions to the data. Figure Figure 15 shows the comparison at t = 0.25 and 0.5 sec. The YAG slab is located between -5 and 5 cm on the graph. While some of the fine structure is lacking, the model tracks the overall temperature rise rather well. Figure Figure 16 shows the comparison at t = 1 and 5 seconds. Once again, the model tracks the date rather well. Finally, in Figure 17 we show the temporal history of a "hot spot" on the surface of the slab. Again, the match-up between the model and the data is quite good.

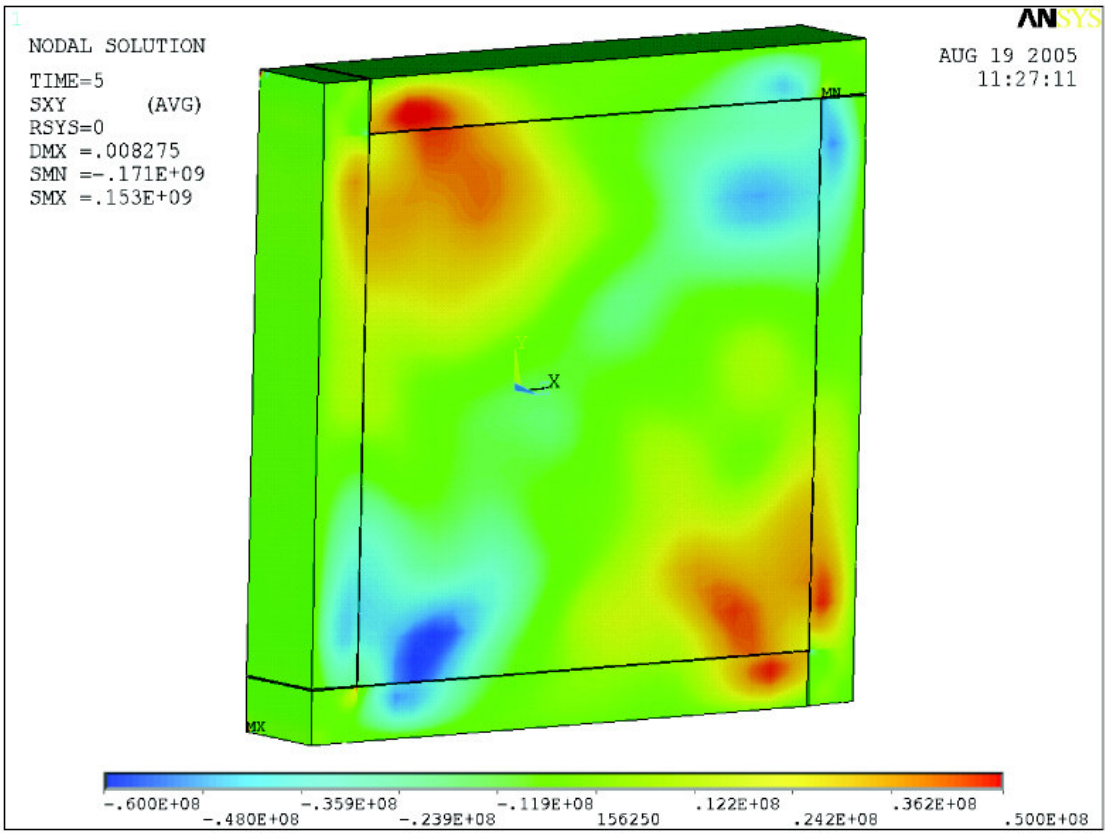

Figure 14: Contours of the X-Y shear stress for the temperature distribution in Figure 13. Scale units are dynes/cm^2; divide by 10^7 to get MPa.

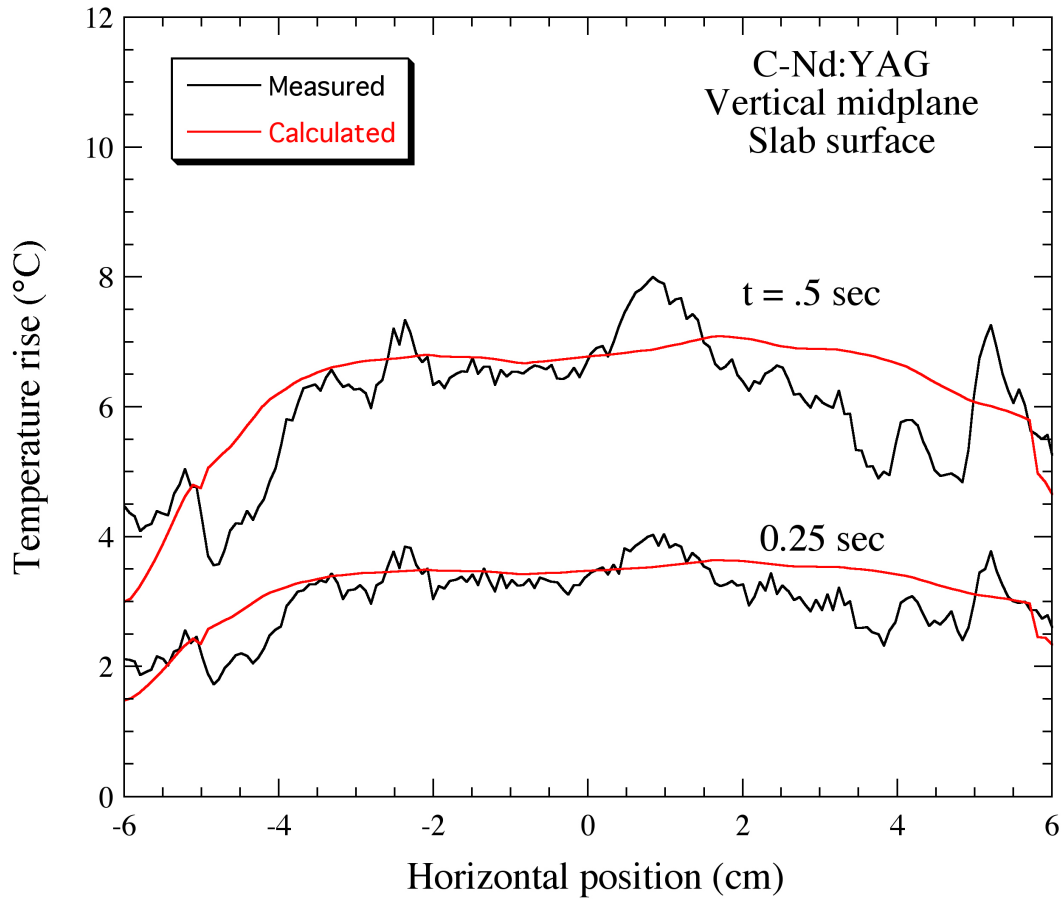

Figure 15: Measured and calculated temperature rises for slab #4.

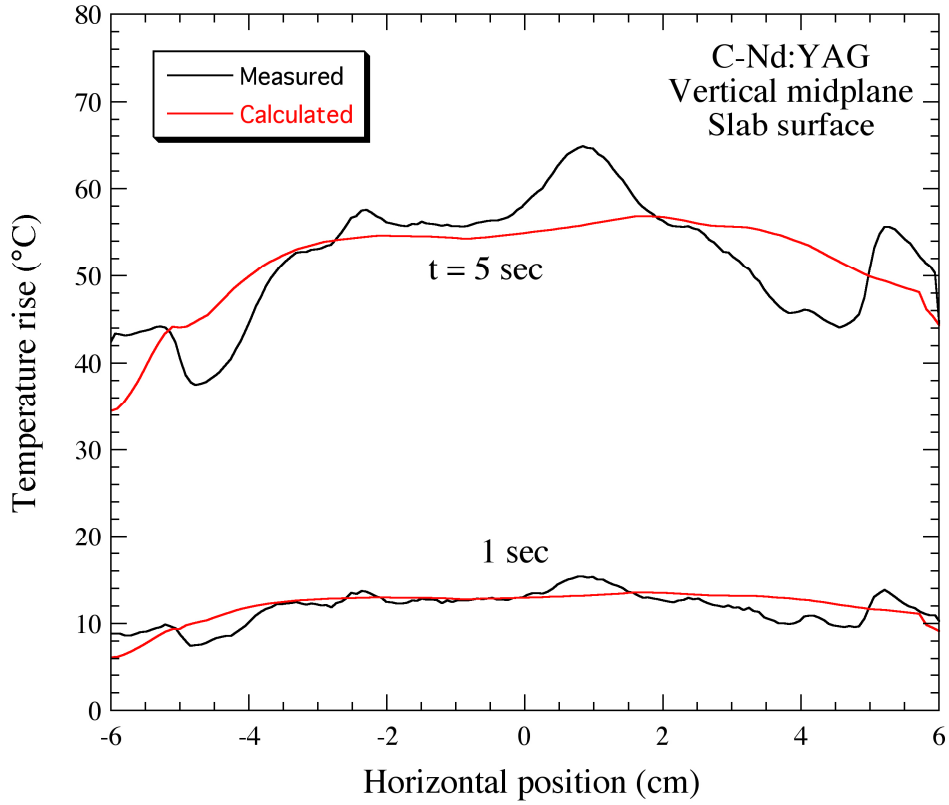

Figure 16: Same as Figure 15 for t = 1 and 5 seconds.

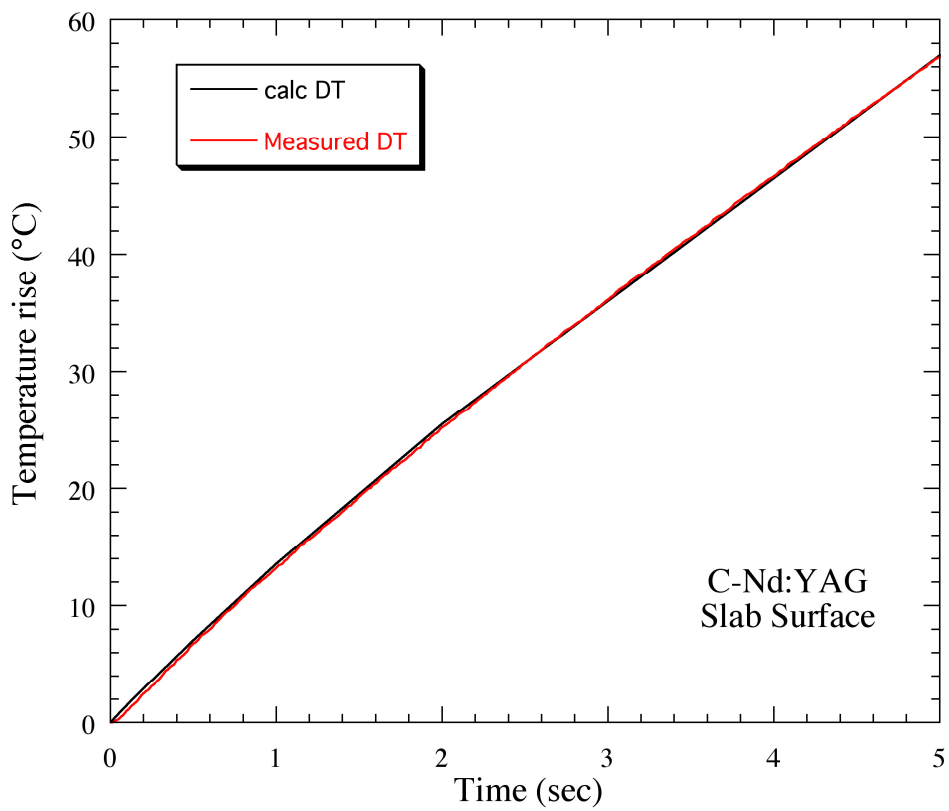

Figure 17: Temperature temporal history for a "hot spot" on the slab surface.

Wavefront calculations

Given the temperature and stress distributions in the laser slabs, we can then calculate the amount of wavefront distortion expected. In general, wavefront distortions come from three sources: 1) The temperature dependence of the refractive index, 2) Mechanical deformation, and 3) Stress-induced birefringence. Stress-induced birefringence also leads to depolarization of an initially linearly-polarized beam. In the following figures, we present the total wavefront phase, and the individual contributions to the total for slab #1.

Figure 18 through Figure 21 show the wavefront phase for slab #1 at t = 0.25 seconds due to all effects, displacement, dn/dT, and stress effects respectively. We note that the vast majority of the wavefront is due to dn/dT and displacement effects; stress effects play a minor role insofar as contributing to the amount of wavefront distortion. Figure 22 through Figure 25 are the analogues for t = 5 seconds. We see that the general pattern observed in the t = 0.25 calculations holds. Units for all the graphs are waves at 1 μm. It turns out that the peak-to-valley (P-V) wavefront distortion does not grow linearly during the five seconds. The P-V value grows linearly during the first second, but then starts flattening out. The P-V value at one second is one wave, whereas at five seconds it is 3.8 waves..

The difference in wavefront for P-polarized and S-polarized light can be traced directly to stress-induced birefringence. The stress contribution to the wavefront in slab #4 at t = 0.25 second for P and S-polarized light is shown in Figure 26 and Figure 27 respectively. We notice that the stress contribution to the wavefront has opposite curvature for P polarization as it does for S polarization. In one case, the stress contribution adds to the overall phase, whereas in the other, it subtracts. This polarization-dependent aberration can impact what one measures for a wavefront since a polarization-insensitive diagnostic (such as a Hartmann sensor) would measure the average of the two polarizations, and thus indicate an essentially flat wavefront. This effect would be more pronounced at early times, where the stress contribution is relatively larger to the overall waverfront than it would be at later times, where its contribution would be less.

The total wavefront due to all four slabs is found to be a coherent addition of the individual slabs. In Figure 28, we give the total wavefront for all four slabs at t = 5 seconds. We notice that there is a substantial amount of curvature to the wavefront. By off-loading spherical correction ($x^2 + y^2$) to another optic(s) (analogous to what is currently done for tip/tilt), the DM would not use up its stroke in correcting sphericity. In Figure 29, we show the wavefront with sphere removed corresponding to the case in Figure 28. We see that the amount of P-V wavefront has been cut in half for almost all times. The table below gives a summary of the total wavefront P-V values found by our calculations.

Time (sec)	Total phase P-V (waves @ 1 μm – four slabs single pass)	Total phase P-V, sphere removed (waves @ 1 μm – four slabs single pass)	Maximum phase gradient (waves/cm)	Maximum phase gradient – sphere removed (waves/cm)
0.25	1.0	0.5	0.5	0.3
0.5	2.0	1.0	1.0	0.6
1.0	3.7	1.8	1.8	1.1
5.0	14.0	8.0	5.3	4.6

The total amount of phase aberration (or gradient) seen at the DM plane is twice the above values, due to double-passing of the slabs. We note that as far as the magnitude of the above aberrations is concerned, we are in reasonable shape; the DM can correct up to sixteen waves. However, what will limit our run time is the gradient. The DM will allow only ±2 μm of relative motion between actuators before freezing. Since there is about one cm between actuators, at a gradient of 2 waves/cm we will have reached our limit. This occurs, from the above table, at about one second run time, or perhaps two seconds with sphere off-loaded to another optic.

Depolarization

For light that is linearly polarized along a given direction, the depolarization value gives the percentage of light that is rotated into the orthogonal polarization. For example, a value of 80% indicates that, at a given point in the aperture, light that is linearly P-polarized emerges from the slab elliptically polarized with 80% of the intensity S-polarized and 20% remaining P-polarized.

As mentioned above, the X-Y shear component of the stress drives the depolarization. Consequently, the spatial distribution of the depolarization tends to follow that of the stress. In Figure 30 and Figure 31 we show the depolarization for slab #1 at t = 0.25 and 5 seconds respectively. We see that, as expected, the majority of the depolarization occurs in the corners of the slab and ranges from less than a percent at t = 0.25 sec to about 80% at t = 5 sec.

The depolarization results for the individual slabs cannot simply be added (or multiplied) to obtain the total depolarization for the four-slab system. The reason is that since the depolarization *intensity* is given, all "phase" information is lost. To compute what would happen for four slabs, the actual Jones' matricies for a given slab must be used. These matricies may be multiplied together to give the results for an arbitrary number of slabs. The results of this calculation for four slabs at t = 5 seconds (single-passed) is shown in Figure 32. Peak depolarization values range from about 10% at 0.25 sec to 100% at 5 seconds. We also note from the five-second data that a substantial amount of the aperture becomes depolarized.

Beam steering

A contour plot of the horizontal and vertical beam steering is shown in Figure 33 for t = 5.0 seconds. The steering angle is given in microradians, with a positive value indicating the beam is steered towards the positive horizontal or vertical axis (the origin of the axes is in the center of the aperture). Let's consider the horizontal beam steering. A positive beam steering angle for negative x-values, and a negative beam steering angle for positive x-values means that the beam is being steered towards positive x on the left side of the aperture and towards negative x on the right side: *i.e.* a converging beam. The same holds true for the vertical beam steering. Lineouts along the vertical midplane (for horizontal steering) or horizontal midplane (for vertical steering) are given in Figure 34. We see that after one second, the maximum steering angle is about 200 μrad (four slabs, single-pass) for both horizontal and vertical steering. A double pass through the slabs would result in a maximum steering of 400 μrad. This value could then be used to determine the actual linear displacement of the beam on the DM, given the path length in the cavity.

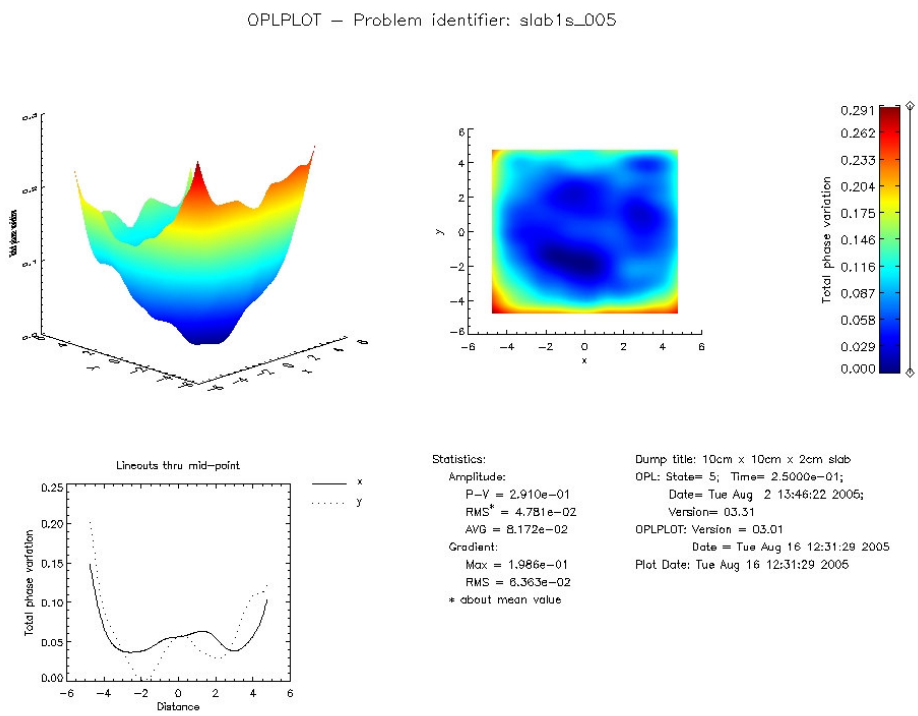

Figure 18: Total wavefront phase for slab #1 at t = 0.25 sec.

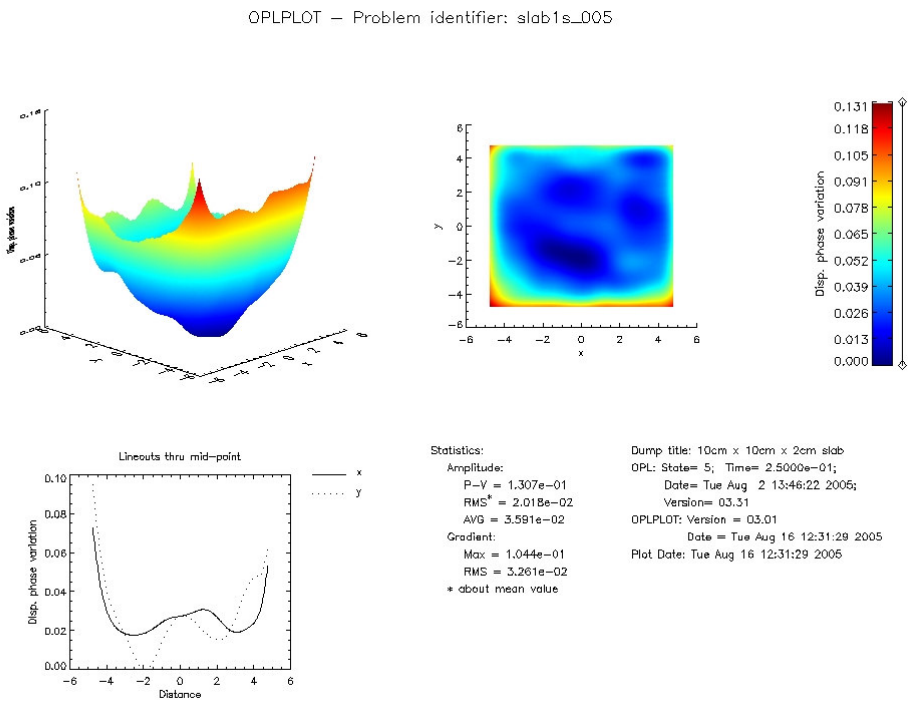

Figure 19: Displacement contribution to wavefront for slab #1 at t = 0.25 sec.

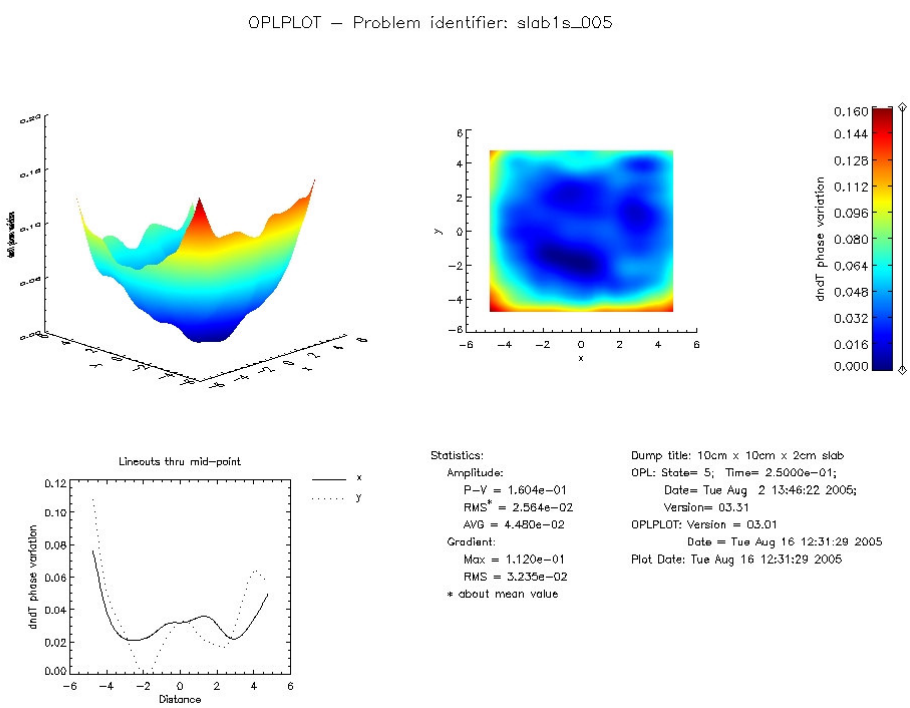

Figure 20: dn/dT contribution to wavefront for slab #1 at t = 0.25 sec.

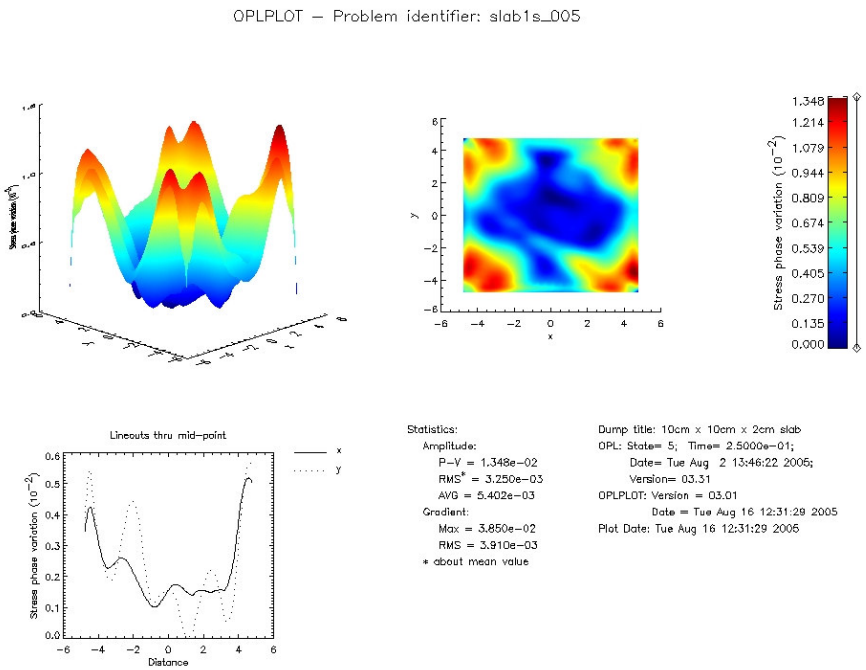

Figure 21: Stress contribution to wavefront for slab #1 at t = 0.25 sec.

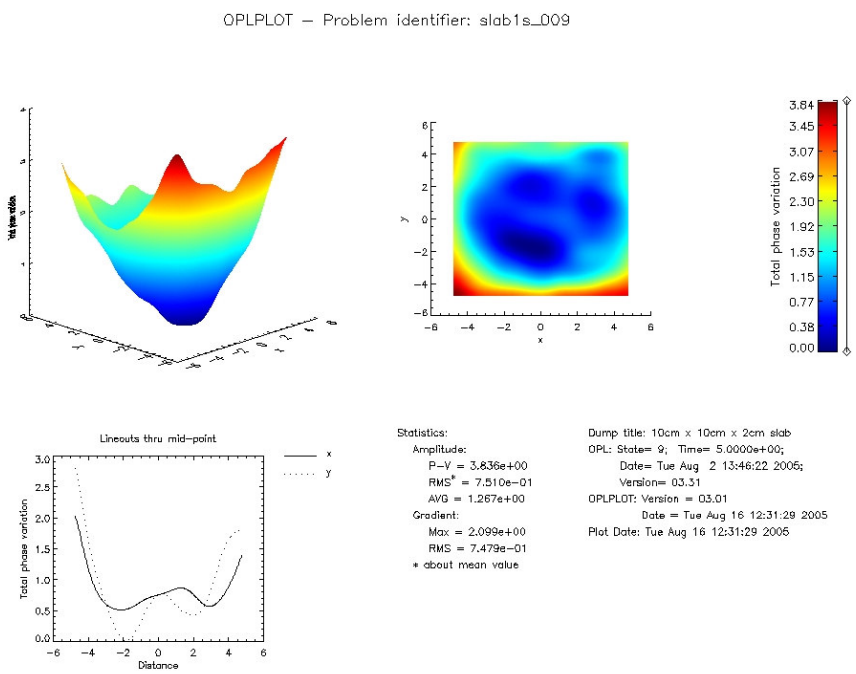

Figure 22: Total wavefront phase for slab #1 at t = 5 sec.

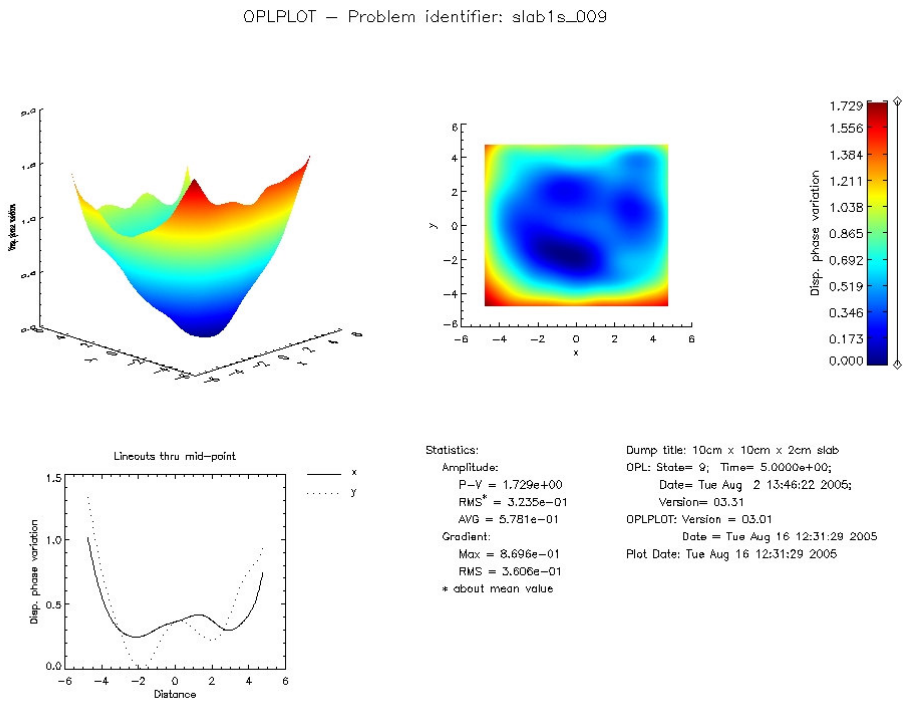

Figure 23: Displacement contribution to wavefront for slab #1 at t = 5 sec.

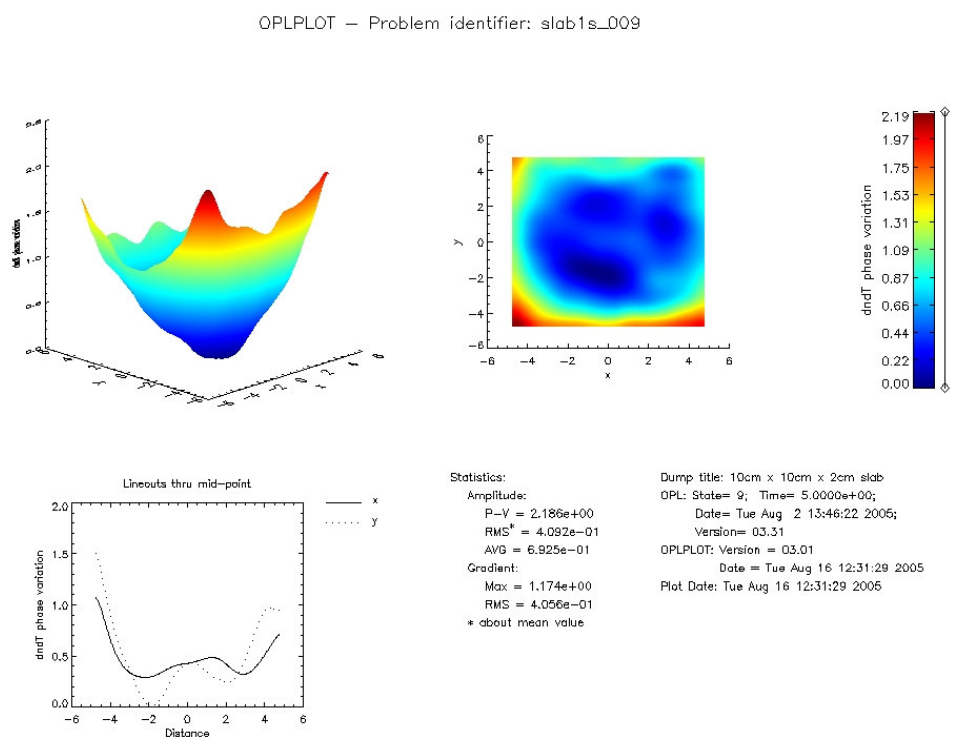

Figure 24: dn/dT contribution to wavefront for slab #1 at t = 5 sec.

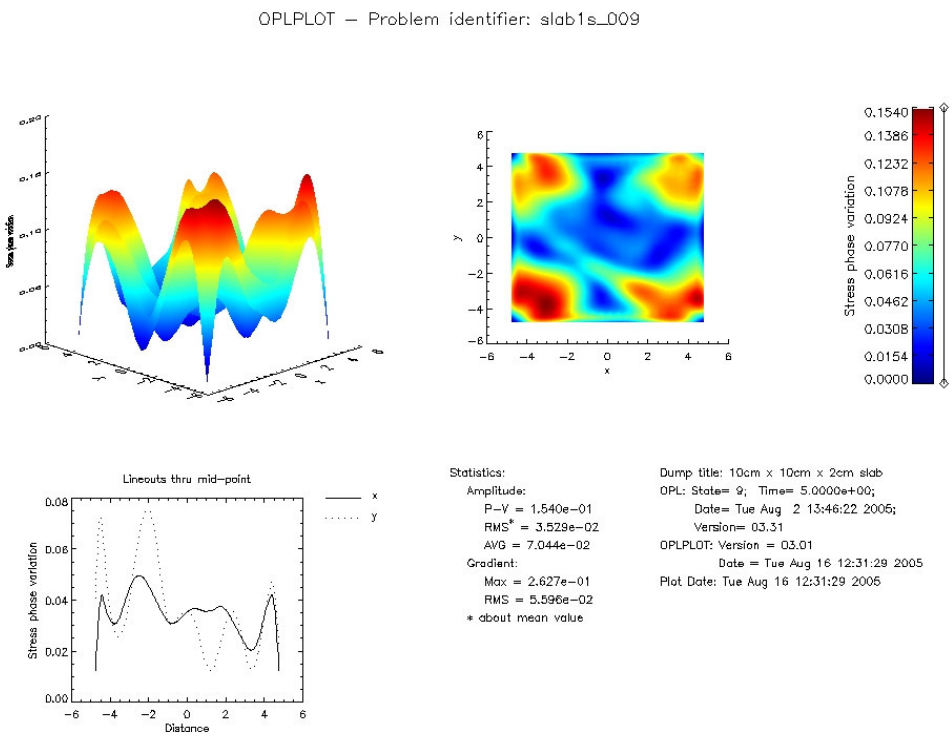

Figure 25: Stress contribution to wavefront for slab #1 at t = 5 sec.

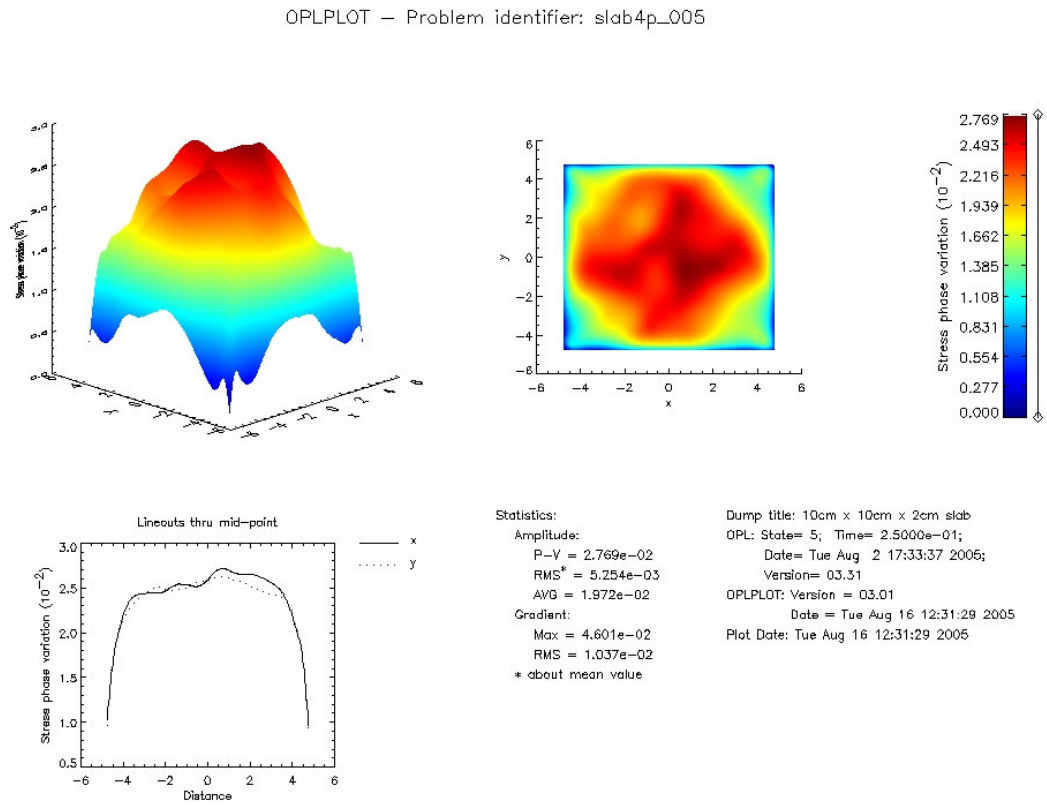

Figure 26: Stress contribution to the wavefront phase for slab #4 at t = 0.25 sec. P-polarized light.

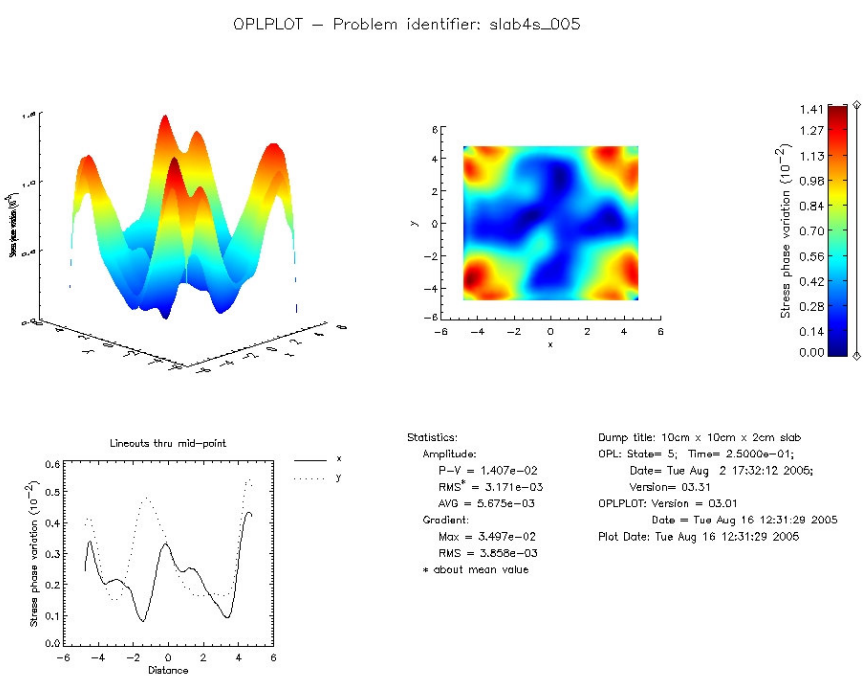

Figure 27: Stress contribution to the wavefront phase for slab #4 at t = 0.25 sec. S polarized light.

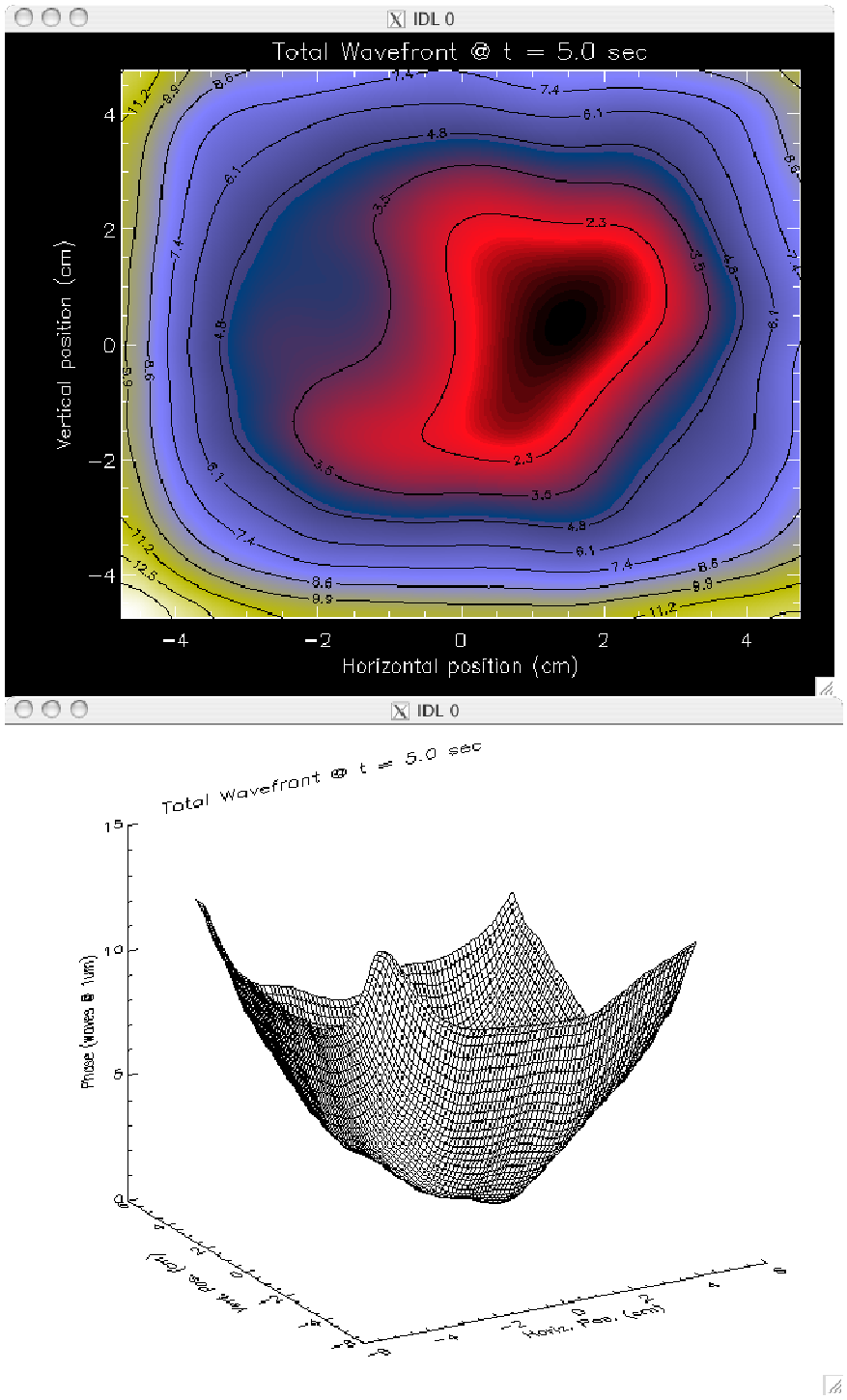

Figure 28: Total wavefront due to four slabs (single-pass) at t = 5 sec.

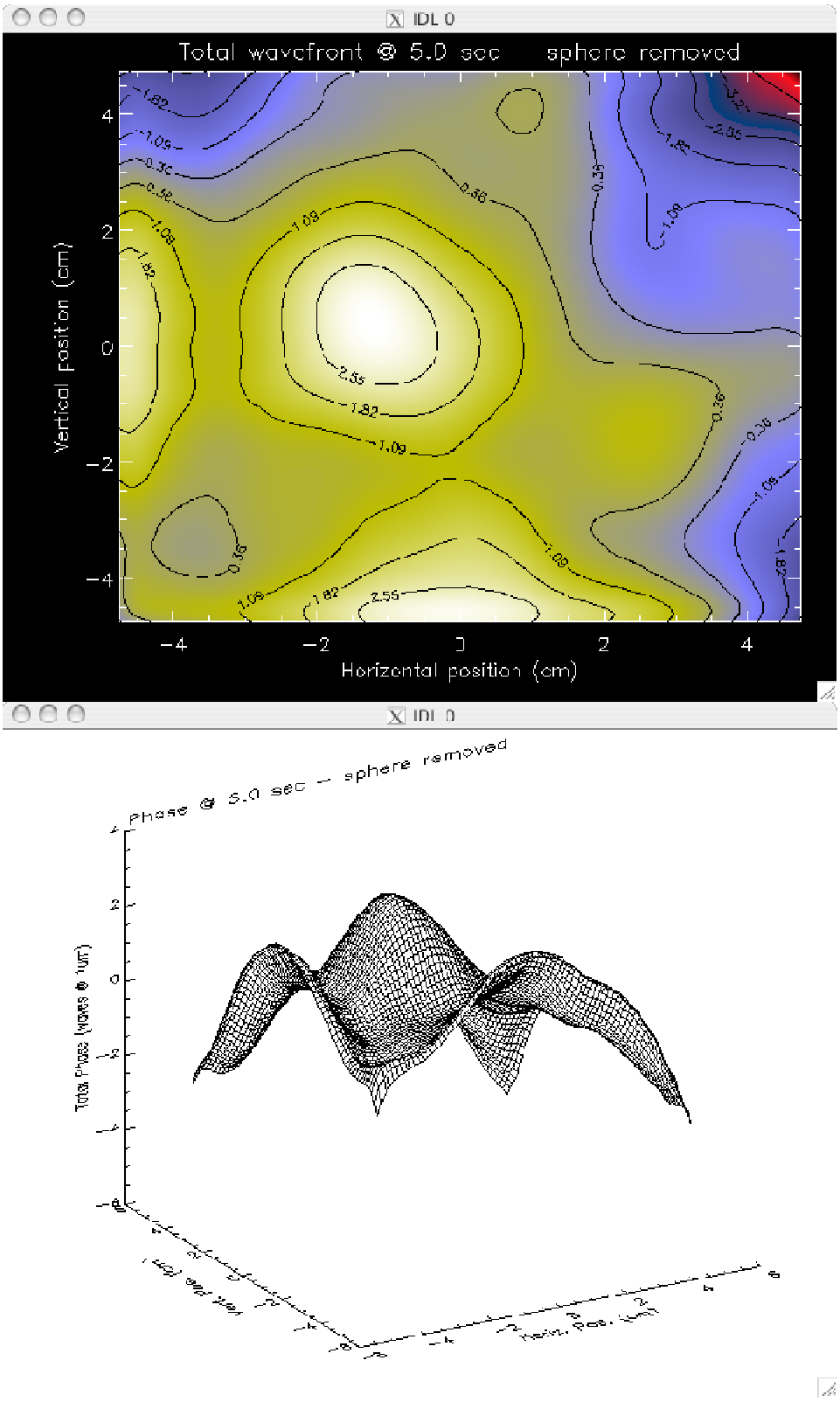

Figure 29: Total wavefront due to four slabs (single-pass) with sphere removed at t = 5 sec.

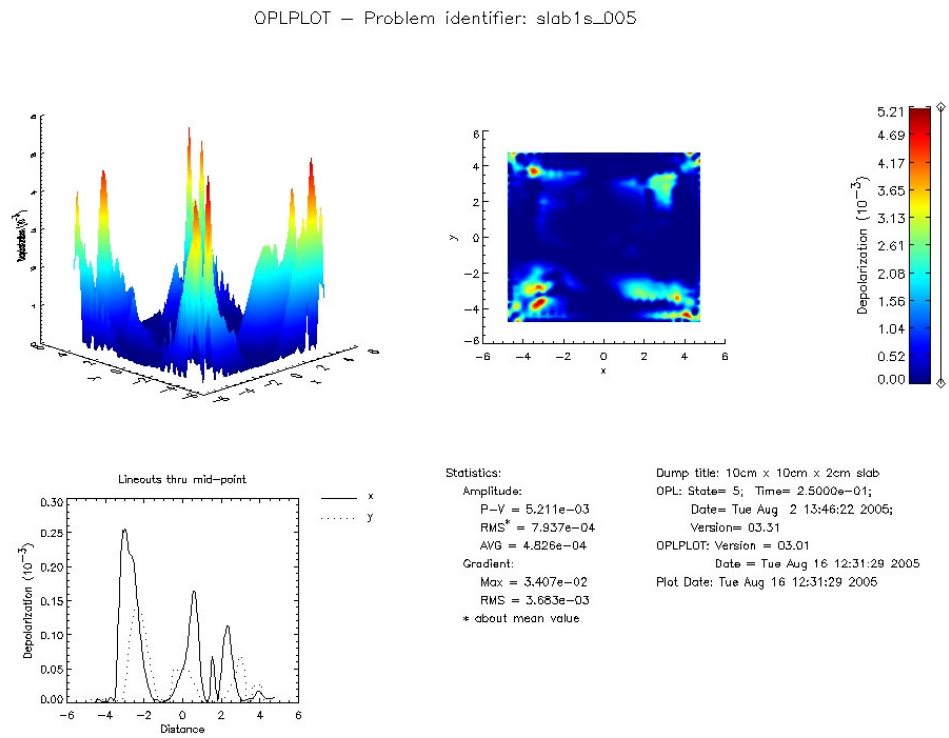

Figure 30: Slab #1 depolarization at t = 0.25 sec

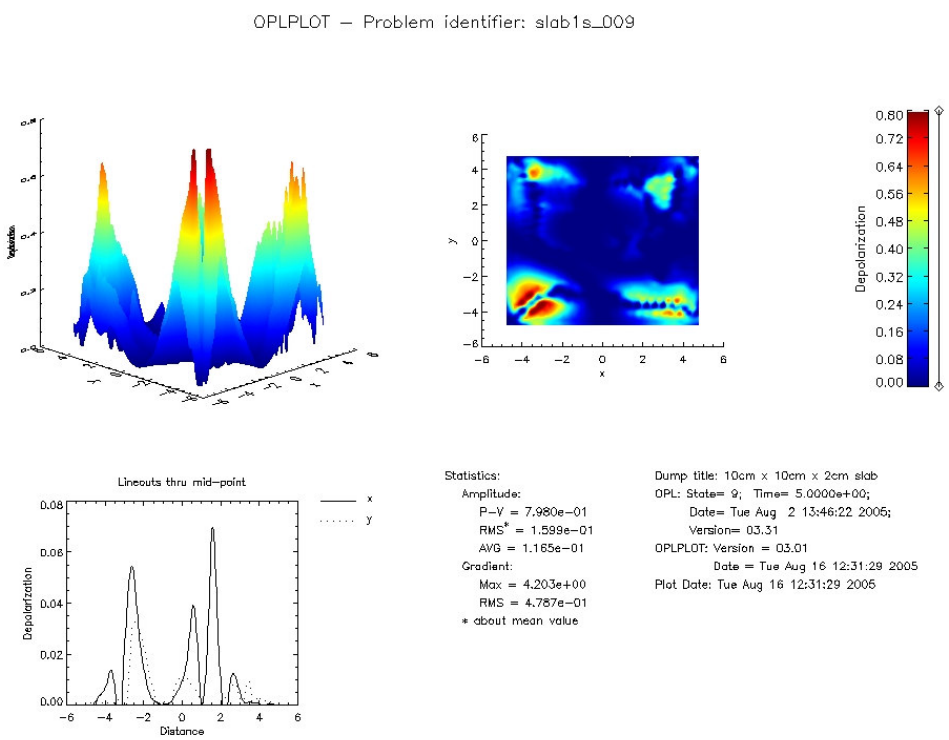

Figure 31: Slab #1 depolarization at t = 5.0 sec

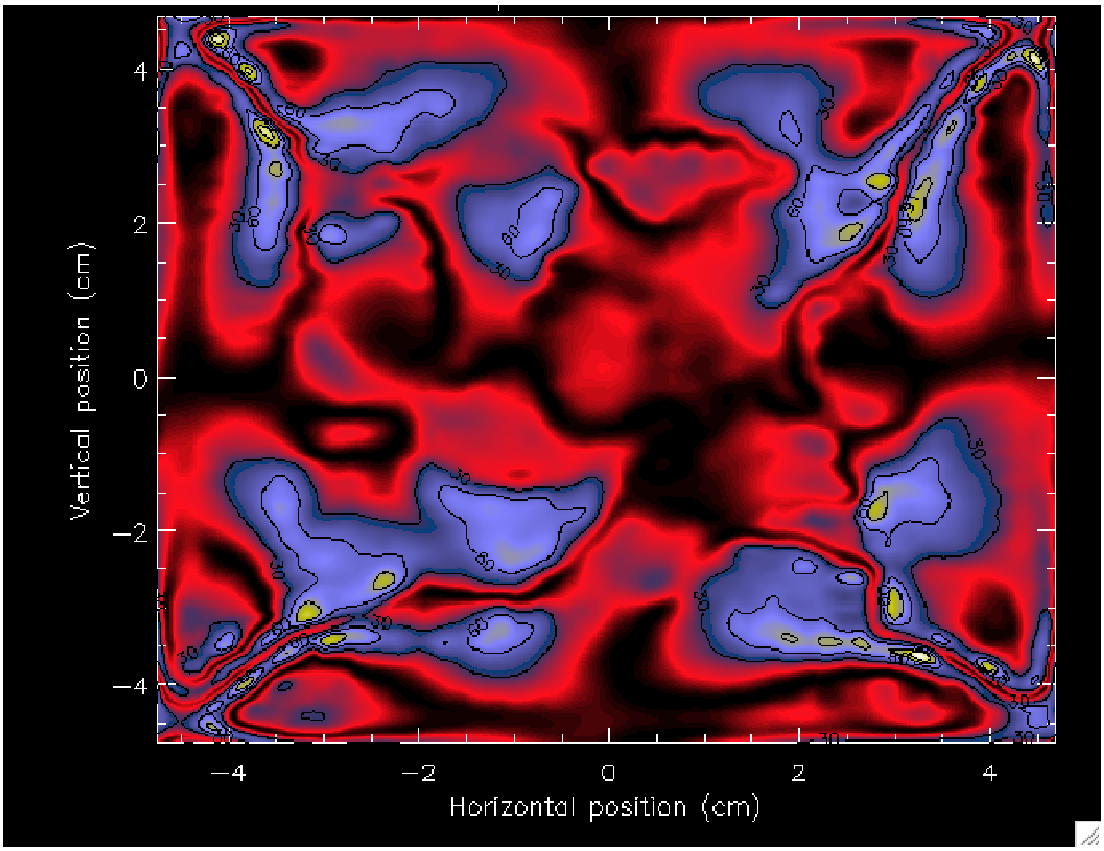

Figure 32: Four-slab (single-pass) depolarization at t = 5 sec.

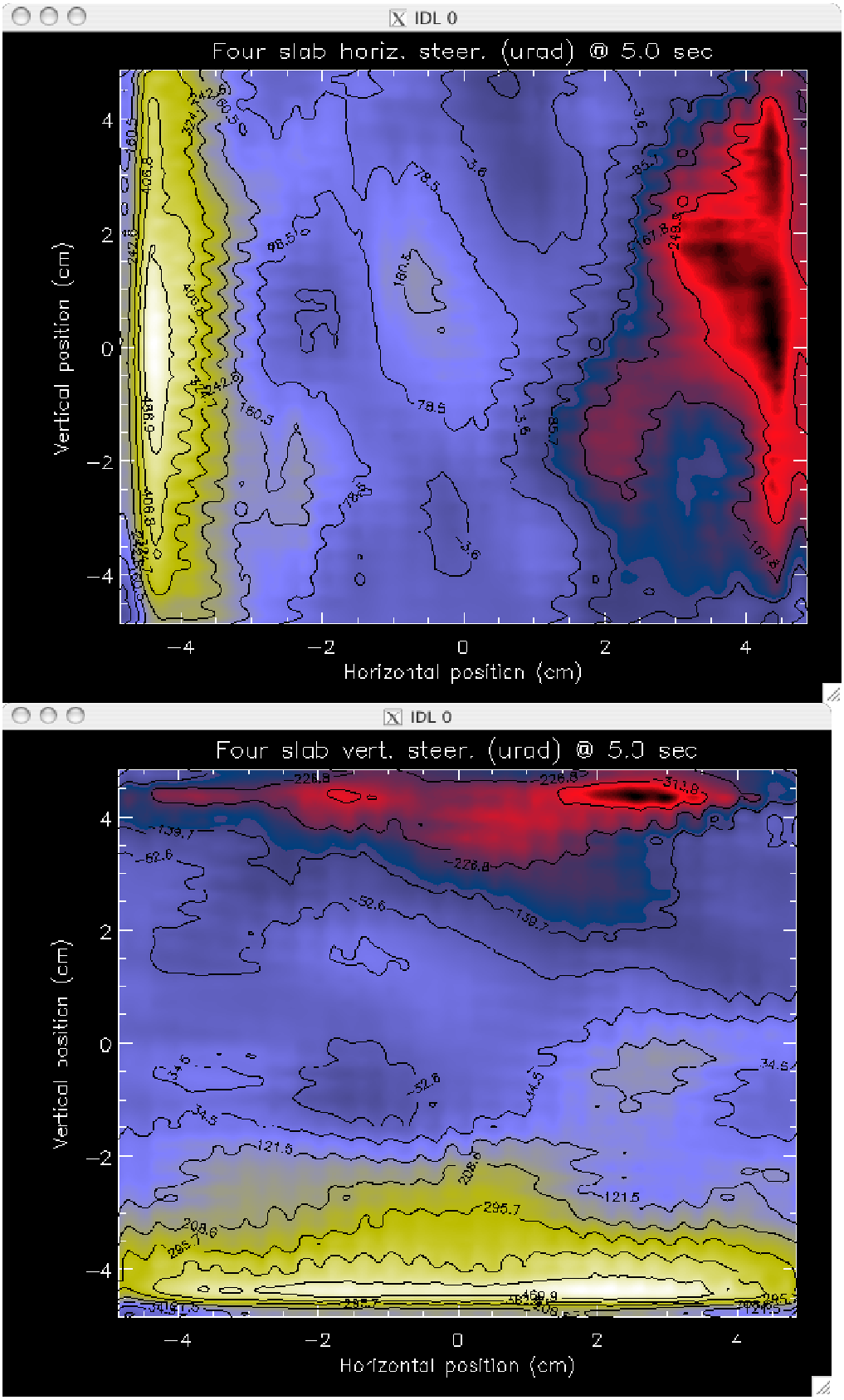

Figure 33: Four-slab (single-pass) steering (μrad) at t = 5.0 sec. Top: Horizontal, Bottom: Vertical

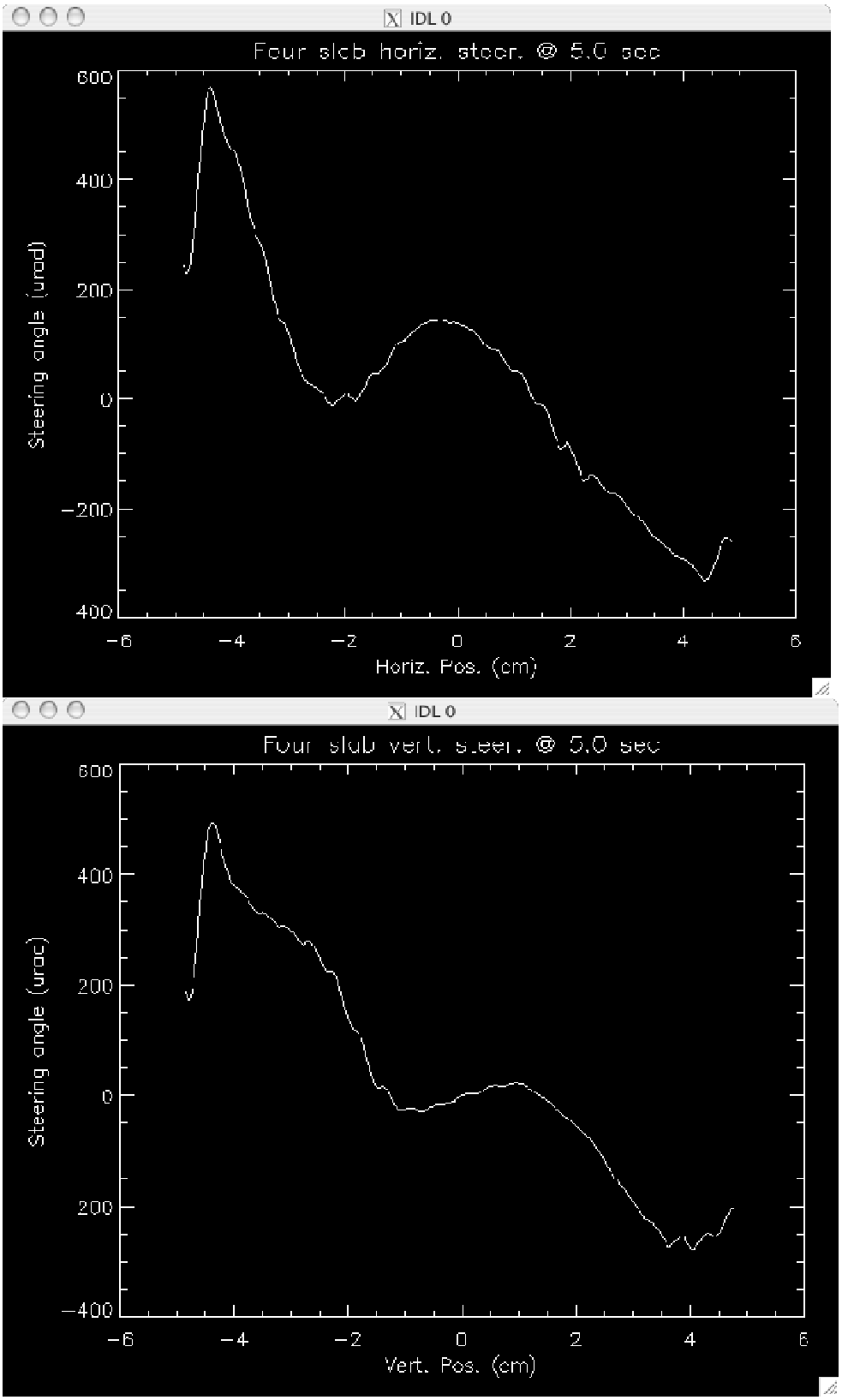

Figure 34: Four-slab (single-pass) steering (μrad) at t = 5.0 sec. Top: Horizontal steering at vertical mid-plane, Bottom: Vertical steering at horizontal mid-plane

Experimental control of wavefront distortions

In order to control the amount of wavefront distortion in the SSHCL, we used a number of techniques. In Figure 35, we show an optical layout schematic of the SSHCL. One of the turning mirrors, and the main method of controlling wavefront, is the intra-cavity deformable mirror (DM). Tip-tilt corrections are applied to the high-reflector, and a quartz rotator midway through the optical chain acts as a birefringence compensator. Not shown in the schematic is the beam sampling plate (placed before the output coupler) and the Hartmann sensor which provides the measurement of the wavefront and provides the signals necessary to control the DM.

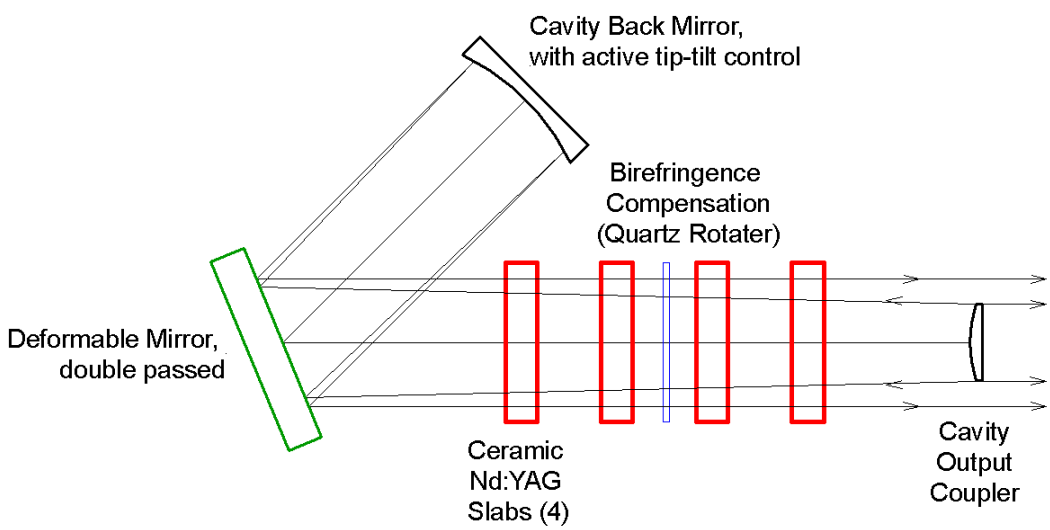

Figure 35: Optical layout schematic of the SSHCL. Not shown are the beam sampling optic (placed before the output coupler) and Hartmann sensor.

As mentioned above, the output beam quality depends very strongly on phase distortions in the resonator. Some of the sources of these distortions include: 1) Pump-induced thermal gradients in the gain medium, 2) Heating of resonator optics by absorbing some of the laser power, and 3) Heating of the environment (surrounding structures and subsequently the atmosphere). We have found that to avoid falloff in beam quality requires wavefront errors be kept below ~35 nm RMS.

The DM is the primary method of aberration control in the SSHCL. A photo of the face of the DM is shown in Figure 36. The optic in front of the DM not only protects the DM proper, but acts to provide a channel for the air knife, which is used to keep dust off the face. The DM is from Xinetics and usues 206 discrete actuators ion a pseudo-hex pattern with ~1 cm spacing. The total stroke limit is $\pm 4\ \mu$m with a maximum inter-actuator stroke limit of $\pm 2\ \mu$m. The DM uses push-pull actuation, and is amenable to "zonal" or "modal" AO correction schemes, but is susceptible to

"print-through." Since the DM is used in a double-passed configuration, the total amount of correction possible is up to 16 waves at 1 μm (low spatial frequency).

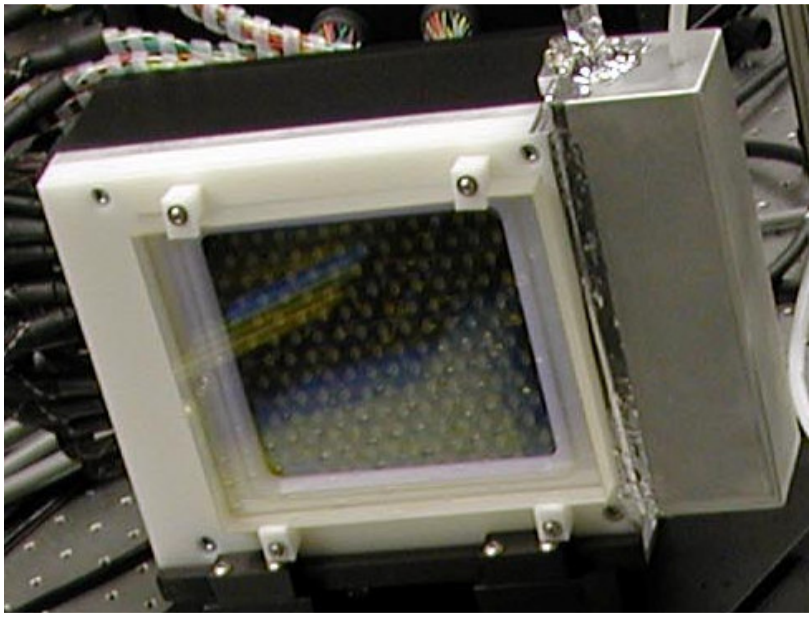

Figure 36: Photo of the front face of the intra-cavity deformable mirror. The actuators can be seen through the front face-plate.

The main source of phase distortions is pump-induced thermal gradients in the gain medium (see Figure 13 for the calculated temperature distribution in the slab). The source of these gradients is primarily non-uniform pump-light deposition on the face of the slab. These non-uniformities get directly imprinted on the wavefront, as shown in Figure 37 below.

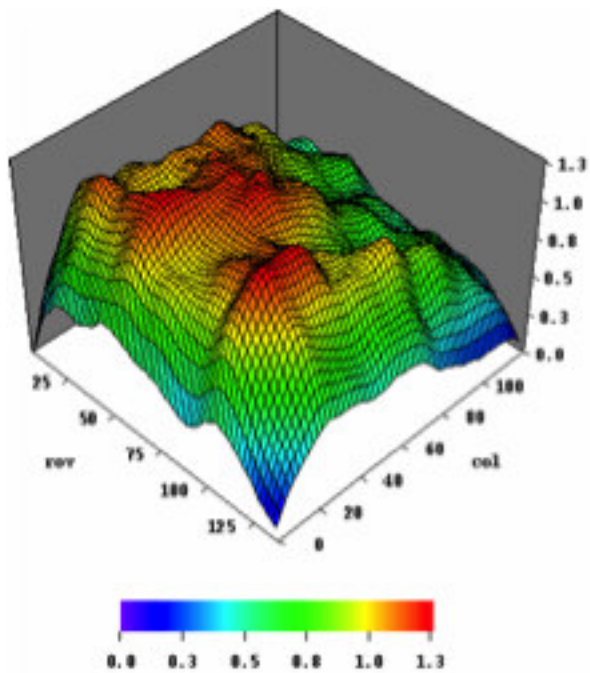

Figure 37: Wavefront due primarily to pump non-uniformity. Scale is in waves at 1.064 μm.

Even though pump non-uniformities produce the greatest effect on wavefront, other effects such as heating of optics or thermally-induced air currents also play a role. For example, the window on the face of the DM was initially BK7 glass. As it turned out, there was unacceptable absorption of the laser light by the window, which caused large amounts of distortion; these distortions were sufficient to be visible in the near-field intensity pattern. We also detected the presence of convection cells via the adaptive-optics control loop. These cells showed up as large tilts that had to be applied to the rear mirror for mitigation. Operating the laser in a Helium atmosphere would be one way to reduce the impact of these cells.

Initially, because of pump non-uniformities and absorption by the DM window, the runtime of the laser was relatively limited – about one second before the level of aberrations was too large to be corrected by the DM. Note this run time is in good agreement with the calculations presented above. By replacing the DM window and using a holographic diffuser in front of the pump arrays, we we able to extend the run time to five seconds at less than 2x diffraction limit, as the following graph shows

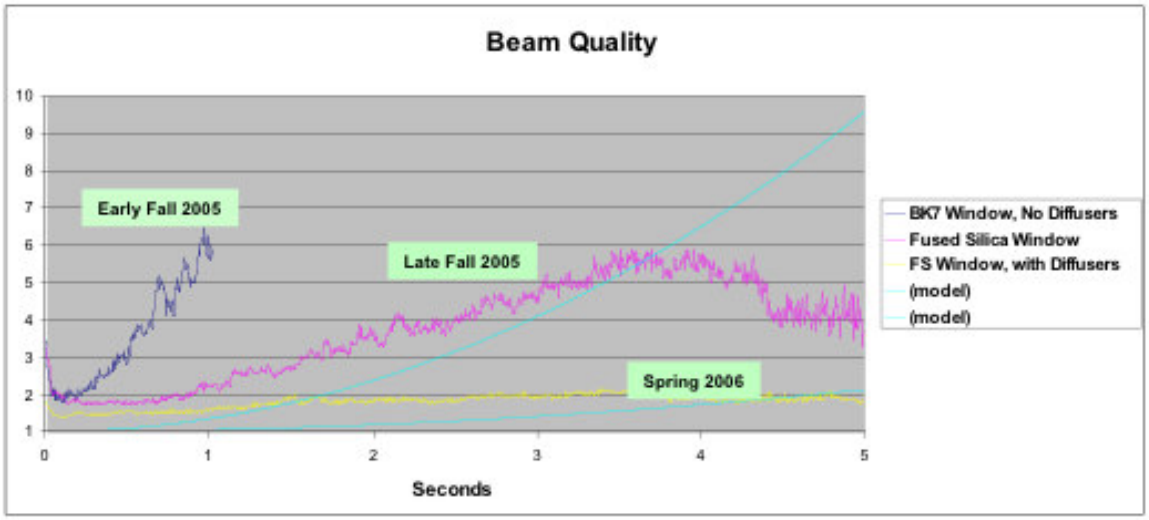

Figure 38: Improvements in beam quality (time diffraction-limit) as a result of changes made to the laser.

The graph labeled "early fall 2005" represents the initial condition of the laser. In "late fall 2005" the BK7 window in front of the DM was replaced with a fused-silica version. In "spring 2006," holographic diffusers were added to the pump arrays. The final result was a beam quality of at most two-times diffraction-limit at the end of the five-second run.

One other approach that has the possibility of providing even better beam quality is by pumping the slab through the edges as opposed to the face. Light ducts from the arrays to the slab would deliver the pump light to the edges, and the light would then propagate through the edge cladding to the active region of the slab. For YAG systems, the use of Samarium-doped edge claddings would be preferred as the pump light would traverse the edge cladding without any absorption; yet the Samarium would absorb the 1.064 μm spontaneous emission, inhibiting parasitics within the slab.

Three benefits of edge pumping are : 1) Improved delivery of pump light to the slab, and hence greater pumping efficiency, 2) Homogenization of the pump light such that non-uniformities would not get impressed onto the wavefront, and 3) Longer absorption path length. This latter benefit would allow pumping at 885 nm, which in turn would result in a smaller quantum defect and hence less heat deposited in the slab. The greater power deposition at the edges of the slab results in a large amount of focus, but the overall profile is smooth, without the high spatial frequencies present in the face-pumped case. See Figure 39 for a comparison between face-pumping and edge-pumping. In principle, a simpler type of adaptive optic system could be used for wavefront control.

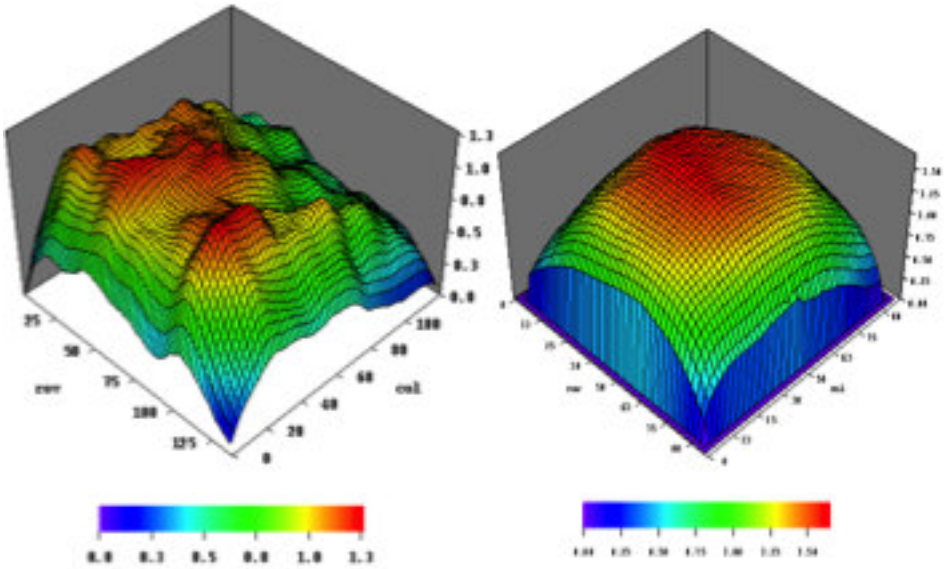

Figure 39: Laser-beam wavefront due to face-pumping (left) and edge-pumping (right).

---

[1] K.S. Jancaitis, *Laser Program Annual Report, UCRL 50021-87,* p. 5-3, Lawrence Livermore National Lab, Livermore, CA, 1987.

[i] P. Beckmann and A. Spizzichino, *The Scattering of Electromagnetic Waves from Rough Surfaces*, Pergamon Press, New York, 1963.

[ii] L. Devroye, *Non-Uniform Ranbdom Variate Generation*, Ch. 2, Springer-Verlag, New York, 1986.

Prepared by LLNL under Contract DE-AC52-07NA27344.